AD-A080538

TECHNICAL
LIBRARY

AD

CONTRACT REPORT ARBRL-CR-00410

PROJECTILE/SABOT DISCARD AERODYNAMICS

Prepared by
Avco Systems Division
201 Lowell Street
Wilmington, MA 01887

December 1979

US ARMY ARMAMENT RESEARCH AND DEVELOPMENT COMMAND
BALLISTIC RESEARCH LABORATORY
ABERDEEN PROVING GROUND, MARYLAND

DTIC QUALITY INSPECTED 1

REPORT DOCUMENTATION PAGE		READ INSTRUCTIONS BEFORE COMPLETING FORM
1. REPORT NUMBER CONTRACT REPORT ARBRL-CR-00410	2. GOVT ACCESSION NO.	3. RECIPIENT'S CATALOG NUMBER
4. TITLE *(and Subtitle)* PROJECTILE/SABOT DISCARD AERODYNAMICS		5. TYPE OF REPORT & PERIOD COVERED Final
		6. PERFORMING ORG. REPORT NUMBER
7. AUTHOR(s) David Siegelman Peter Crimi		8. CONTRACT OR GRANT NUMBER(s) DAAK11-77-C-0080
9. PERFORMING ORGANIZATION NAME AND ADDRESS Avco Systems Division 201 Lowell Street Wilmington, MA 01887		10. PROGRAM ELEMENT, PROJECT, TASK AREA & WORK UNIT NUMBERS
11. CONTROLLING OFFICE NAME AND ADDRESS US Army Armament Research & Development Command US Army Ballistic Research Laboratory (DRDAR-BL) Aberdeen Proving Ground, MD 21005		12. REPORT DATE DECEMBER 1979
		13. NUMBER OF PAGES 85
14. MONITORING AGENCY NAME & ADDRESS*(if different from Controlling Office)*		15. SECURITY CLASS. *(of this report)* UNCLASSIFIED
		15a. DECLASSIFICATION/DOWNGRADING SCHEDULE

16. DISTRIBUTION STATEMENT *(of this Report)*

Approved for public release; distribution unlimited.

17. DISTRIBUTION STATEMENT *(of the abstract entered in Block 20, if different from Report)*

18. SUPPLEMENTARY NOTES

19. KEY WORDS *(Continue on reverse side if necessary and identify by block number)*

Sabot Discard
Launch Dynamics
Sabot Interactions
Fin-Stabilized Projectiles

20. ABSTRACT *(Continue on reverse side if necessary and identify by block number)*

An engineering analysis procedure which describes the sabot discard process for gun-launched projectiles has been modified in order to provide an improved tool for investigating the effects of sabot, projectile and launch parameters upon near field dispersive forces. Experimental test data generated by BRL has been used to formulate an improved engineering model of the interaction flow field which develops about the projectile/sabot petal package during the removal process. The experimental data indicated that individual compression

(cont'd)

DD FORM 1473 EDITION OF 1 NOV 65 IS OBSOLETE
1 JAN 73

20.   (cont'd)

wave intersections and reflections are present within the annular flow passage.
In order to model this behavior, an integrated flow element approach utilizing
local shock/expansion procedures has been evolved.

FOREWORD

This study was conducted by Avco Systems Division for the
U. S. Army Ballistic Research Laboratories under Contract No.
DAAK11-77-C-0080. Technical Monitor for BRL was
Dr. Edward M. Schmidt. Program Manager for Avco Systems
Division was Dr. William G. Reinecke.

TABLE OF CONTENTS

ILLUSTRATIONS

LIST OF SYMBOLS

A	Cross sectional area for one dimensional duct flow
l	Length of sabot underside
Δl	Incremental length to throttling shock location
M	Mach number
P	Pressure
R_{eff}	Effective nose radius
x	Axial position along projectile
y	Lateral position
Δy	Separation distance between sabot and projectile at outlet
z	Axial coordinate along sabot
α	Sabot pitch angle
δ	Sabot face angle
φ	Pressure scaling function
θ_s	Shock wave angle
τ	Sabot thickness

Subscripts

1	Background level on sabot underside
2	Value downstream of shock wave
NS	Static value downstream of normal shock wave
t	Stagnation value downstream of normal shock wave
CRIT	Critical value for throttling of duct flow
end	Value at outlet station

Superscripts

*	Value at sonic conditions

1.0 INTRODUCTION

The trajectory of a gun-launched projectile can be adversely affected by disturbances in the vicinity of the muzzle. In particular, projectiles launched with the aid of a sabot can be subjected to asymmetric forces and moments associated with the sabot discard process which could be significant contributors to dispersion. Recently, an engineering analysis was developed which describes sabot discard dynamics and the resulting loadings on the projectile, in order to provide a tool for assessing the influence of sabot, projectile and launch parameters upon projectile disturbances imparted in the vicinity of the muzzle.[1]

Aerodynamic interaction was found to be the key element of the overall system representation, as the sabot separation process was initially dominated by interactive aerodynamic effects. The complexity of the problem dictated that considerable simplification be employed in the anlytical development, the principal assumption being that the flow between a given sabot segment and the projectile was basically uniform. Results of analyses of one specific configuration agreed qualitatively with photographic records of the sabot separation process, but there were significant quantitative differences which remained to be resolved. These differences were attributed primarily to the approximations made in the

aerodynamic interaction model, indicating that further development of analytical representations of the sabot discard process required improvement of the aerodynamic interaction flow field model.

2.0 INTERACTION FLOW FIELD

In order to better understand the nature of the interaction flow field which develops when the projectile and sabot petal are in close proximity, BRL recently conducted a detailed wind tunnel test program at the NASA Langley test facility.[2] The test conditions and model geometry are summarized in Figure 1. Typical test results are presented in Figures 2 - 5 in order to illustrate the following features of the interaction flow field.

(1) When the projectile and sabot are in close proximity, there is a complex flow pattern involving flow separation and shock intersection developed over the projectile tip/sabot cup region. This is indicated by the overshoot of normal shock recovery pressure observed on the projectile surface and the non-monotonic shape of the sabot cup face pressure shown in Figure 2. Note that separation also extends forward onto the conical projectile tip. This type of spiked body flow has been studied in detail elsewhere for both steady and unsteady flow configurations.[3 - 6]

(2) As the separation distance between the projectile and the sabot petal increases, the individual shock wave intersections become more evident as seen in Figure 3. The peak pressure on the projectile surface is due to impingement of the sabot bow shock, while the peak pressure on the

$M_\infty = 4.5$ $Re_\infty = 2.0 \times 10^6$ 1/FT.

$Pt_\infty = 34.6$ LB/IN^2 $T_t = 175^\circ$ F
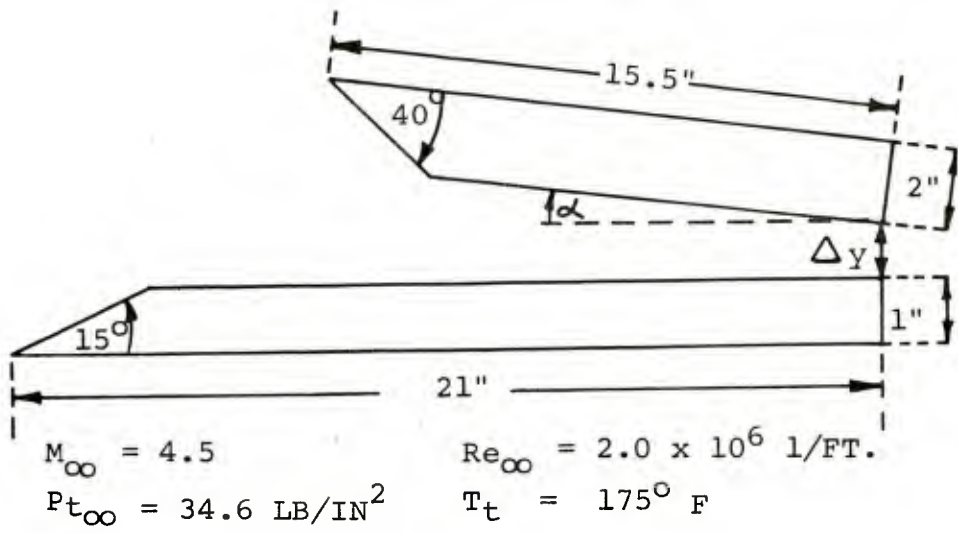
TEST NUMBER										
ΔY (IN) / α (°)	0	2	4	6	8	10	12	14	16	18
.128	107									
.5	108	124	134	142	150	158	168	176		
1	109	123	133	140	149	157	167	175	183	190
1.5	110	122	132	141	148	156	166	174	182	189
2.0	111	121	131	139	147	155	165	173	181	188
2.5	112									
3.0	113	120	130	138	146	154	164	172	180	187
3.5	114									
4.0	115	119	129	137	145	153	163	171	179	186
4.5	116									
5.0		118	128	136	144	152	162	170	178	185
6.0			127	135	143	151		169	177	184

FIGURE 1   EXPERIMENTAL TEST CONFIGURATION

1-1689
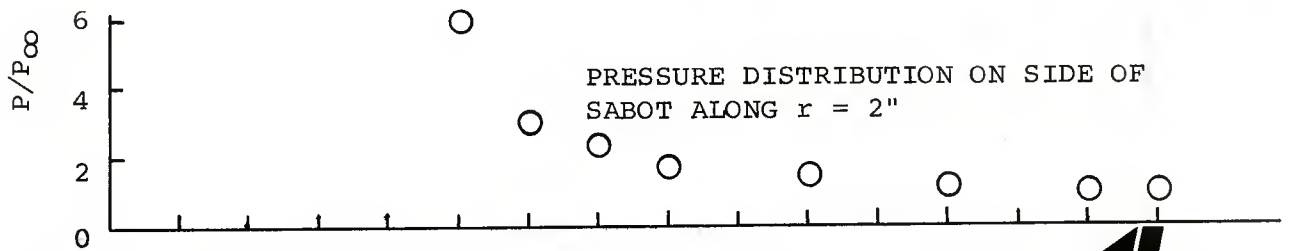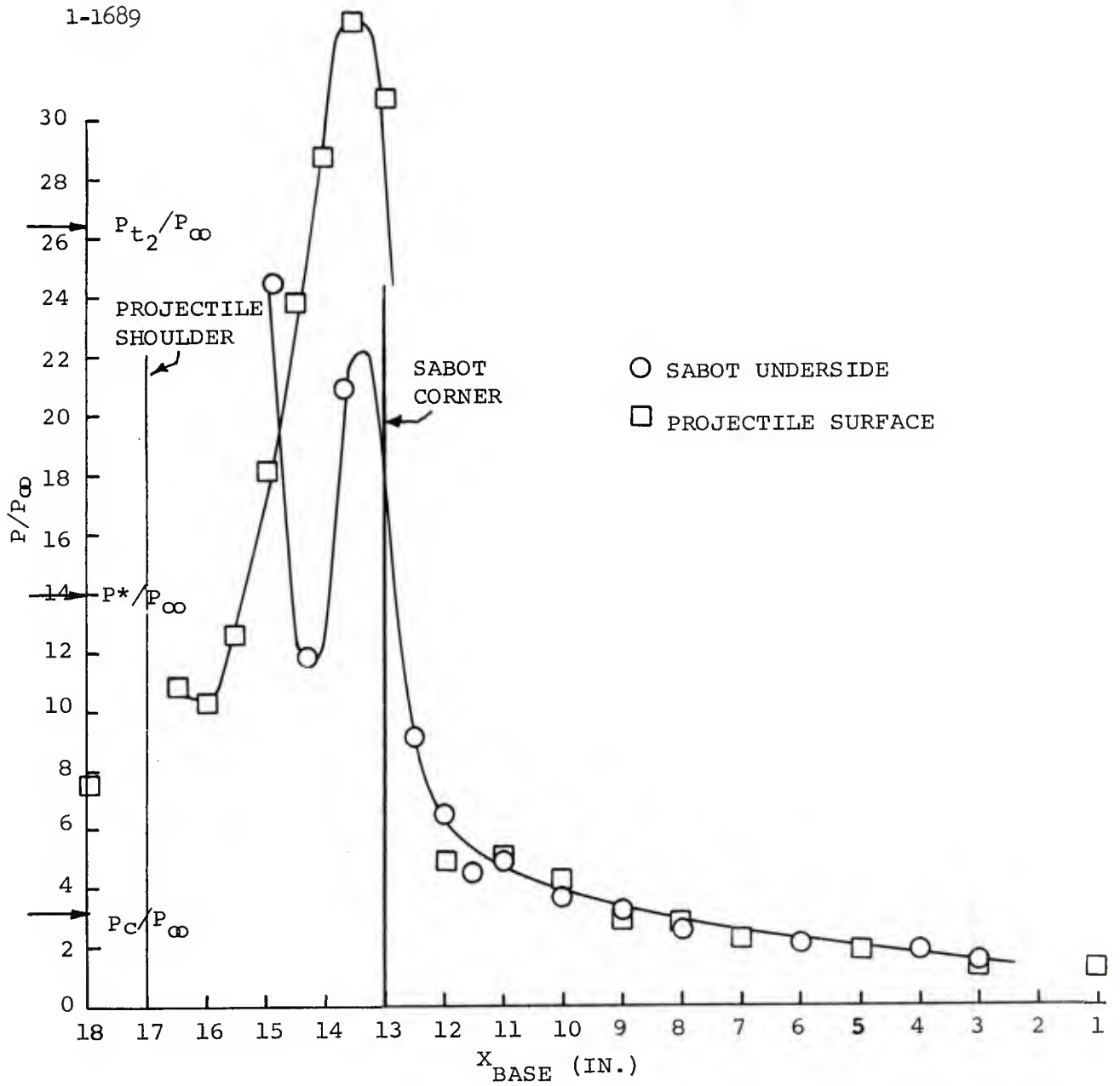
FIGURE 2 - PRESSURE DISTRIBUTIONS FOR PT108, $\alpha = 0°$ and $\Delta Y = 0.5$ IN.
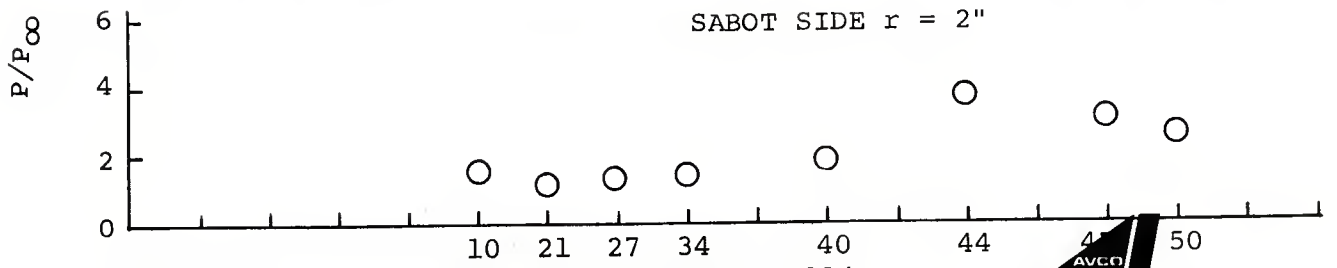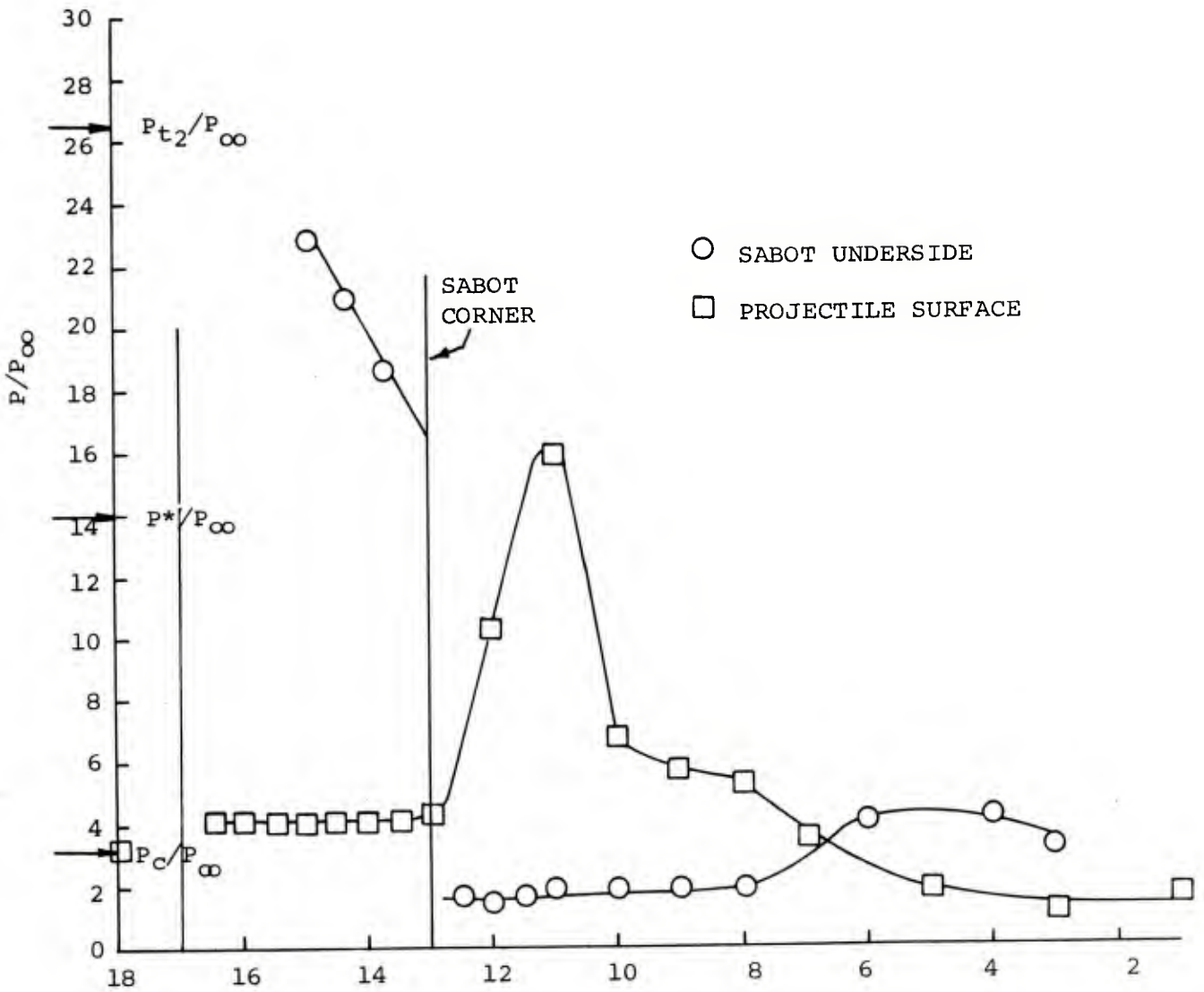
FIGURE 3 - PRESSURE DISTRIBUTIONS FOR PT 114,
$\alpha = 0°$ AND $\Delta Y = 3.5$ IN.

sabot underside is due to impingement of the reflection of this wave off of the projectile surface. Regions of boundary layer separation about these impinging waves are also evident.

(3) The pressure distribution on the lateral sabot edges closely follows the sabot underside behavior.

(4) As the sabot petal pitches up, there is a tendency for pressure levels to rise substantially in the vicinity of the outlet station on both the sabot petal underside and the projectile surface (see Figures 4 - 5). The pitching motion displaces the sabot bow wave origin laterally resulting in impingement of weaker waves and producing lower pressures as seen in Figure 5. The pitch-up results in increased wave strength and pressure rise on the sabot underside, however.

FIGURE 4 - SABOT PETAL UNDERSIDE PRESSURE DISTRIBUTIONS

1-1689

-8-
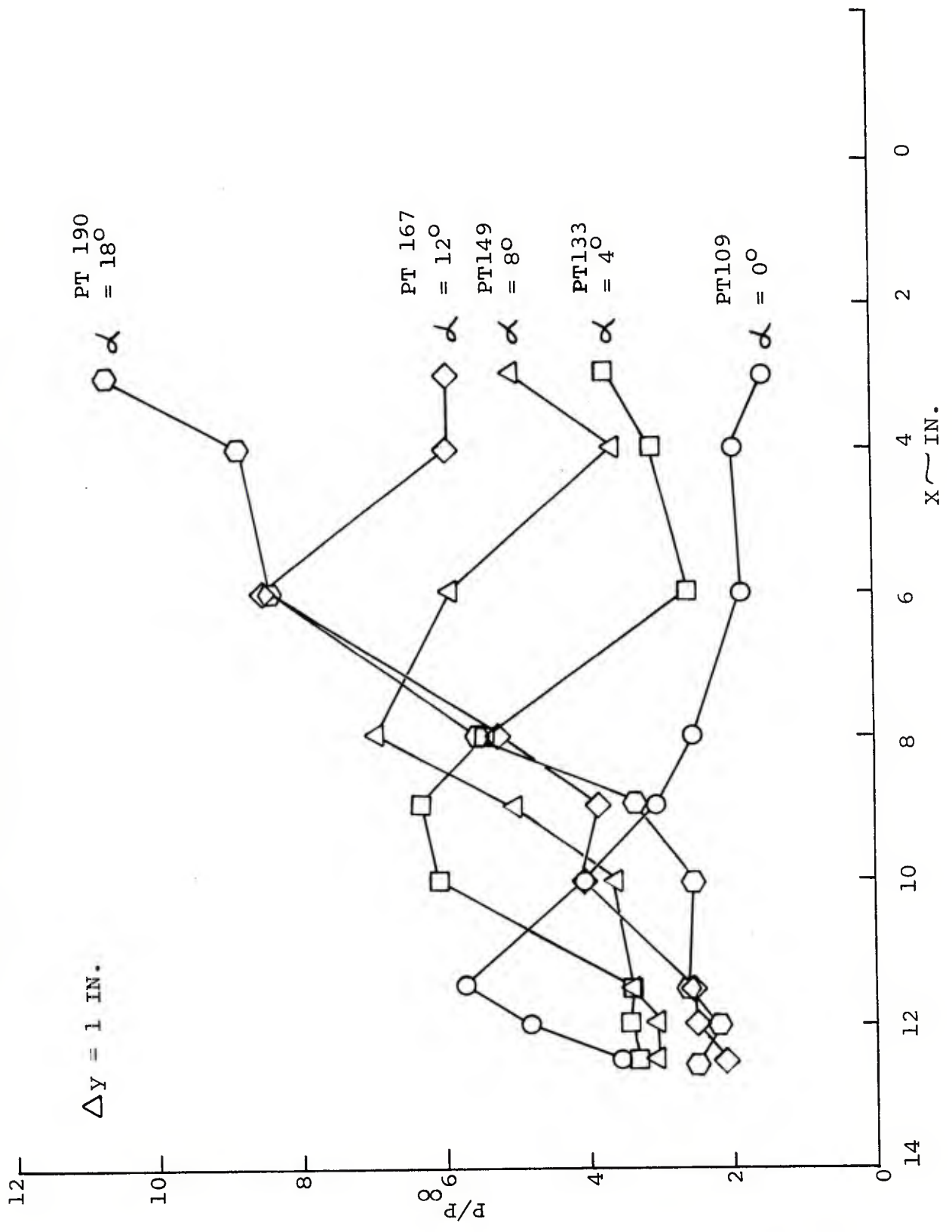
FIGURE 5 - PROJECTILE SURFACE PRESSURE DISTRIBUTIONS

$\Delta y = 1$ IN.

1-1689
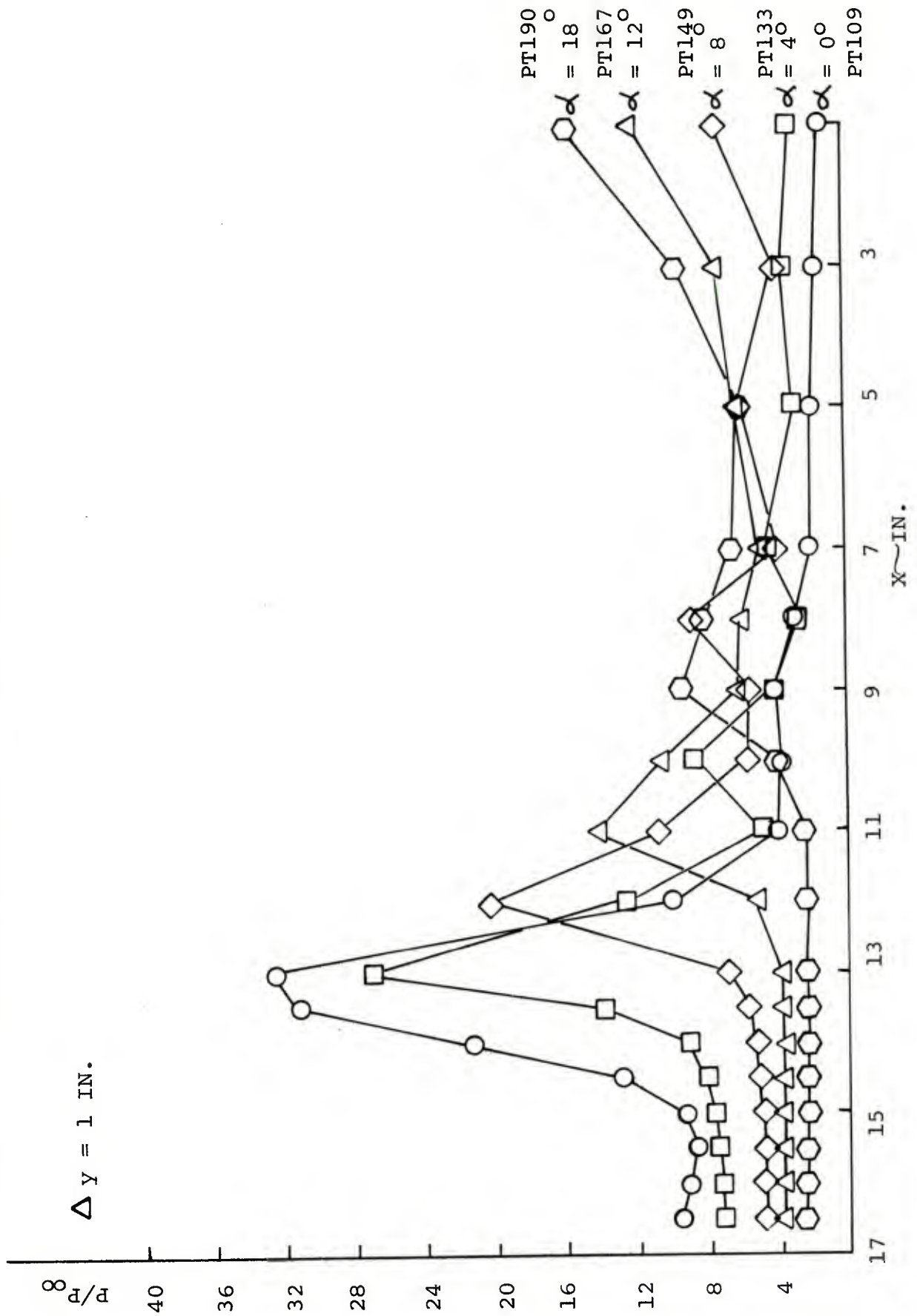
3.0 ENGINEERING MODELING

It is particularly evident from the experimental results presented in Figure 3 that the interaction flow field cannot be modeled as a simple one-dimensional channel flow. That is, the upper-wall and lower-wall pressures are generally different at a given station. For this reason, it was decided to model the overall interaction flow field by integrating appropriate local compression and/or expansion modules.

3.1 SABOT CUP PRESSURE MODEL

The sabot cup pressures have been modeled in the following manner.

(1) For cases where the effective sabot cup face angle (geometric angle plus angle of attack) exceeds the critical value for an attached bow shock wave to be present at the given freestream Mach number, a detached wave pattern will be present. The sabot cup pressures will then approximate those on a blunt obstacle. This analogy has been used to construct a simple engineering model for the cup pressure levels. The cup leading edge is equated to the stagnation point of the analogous blunt obstacle and the pressure is therefore set at the normal shock recovery value.[7] The sabot corner is equated to the sonic point on the analogous blunt obstacle and the pressure is set at the sonic

value of the normally shocked ambient flow.[7] A parabolic
pressure distribution is then generated by use of these two
pressure values plus the condition that the pressure gradient
is zero at the leading edge (i.e.: stagnation point)[8].

(2) For cases where the effective sabot cup face angle
permits an attached shock wave to be present, oblique shock
relations are used to find the (constant) face pressure level.[7]

(3) For cases where the gap between the sabot under-
side and the projectile surface at the sabot corner station
is insufficient to pass the captured mass flow (at sonic
conditions corresponding to the normally shocked ambient flow),
the flow must spill over the sabot and the bow wave will
be detached. Thus, sabot cup face pressures are evaluated
as in case (1), even if the effective sabot cup face angle
were small enough to allow an attached wave solution for a
free flying situation.

(4) The total lateral force on the sabot face cup is
also evaluated using Newtonian flow approximations.[8]
Whenever the Newtonian force prediction exceeds that ob-
tained using the interaction model values, the sabot cup
face is deemed to be in free flight and the Newtonian
values are used.

(5) No attempt has been made to model non-monotonic
pressure behavior of the type seen in Figure 2 because the

present approach furnishes reasonably good average pressure values and also because implementation of such more detailed flow modeling procedures[4-5] would require a degree of complexity inconsistent with the charter of these ongoing development activities.[1]

3.2 SABOT UNDERSIDE PRESSURE MODEL

There are essentially four features of the sabot underside pressure distribution which require modeling.

(1) The background level of pressure must be computed. This value is obtained by performing a Prandtl-Meyer expansion[7] of the sabot cup face flow through the geometric face angle in order to turn the face flow tangent to the sabot underside.

(2) The next step is to estimate the (reference) level of the peak pressure bump observed on the sabot underside at zero incidence (see Figure 3). This pressure bump has been ascribed to boundary layer separation caused by impingement of the sabot bow shock reflection back off of the projectile surface. Therefore, turbulent separation data[9] was used to estimate the magnitude of this peak value via:

$$P_{sep}/P_1 = 1 + (M_1 - 1)^{3/2}$$

(3) The third issue involves locating and sizing this pressure bump. Although it is well-known that separation

length scales are in proportion to the local approach flow boundary layer thickness,[9-11] a purely inviscid description of the bump geometry was sought in order to avoid further complicating the flow modeling subroutines of the sabot dynamics code. A relatively rigorous approach for defining the shock impingement geometry involves construction of an approximate sabot bow shock, location of the shock-projectile impingement point, determination of the initial reflected shock strength and subsequent tracing of the reflected shock back up to the sabot underside. In fact, it was found necessary to carry out much of this procedure in order to adequately estimate the separation pressure rise observed on the projectile surface (see Section 3.3). Determination of the extent of the elevated pressure zone would remain to be modeled empirically.

This issue was considerably simplified by use of the procedure illustrated in Figure 6. Here, the sabot face is projected down to the projectile surface and a Mach wave is reflected back up to the sabot underside. The intersection of this Mach wave with the sabot underside serves to define the end of the pressure pulse (E), while the projectile intersection point serves to define the start of the pressure pulse (S). A triangular pressure pulse centered between these points serves to complete the pressure pulse description.*

_____

*Note that in those cases where the sabot bow shock was found to not impinge upon the projectile surface (see Section 3.3, part (3)), this pressure bump on the sabot underside was also deleted.
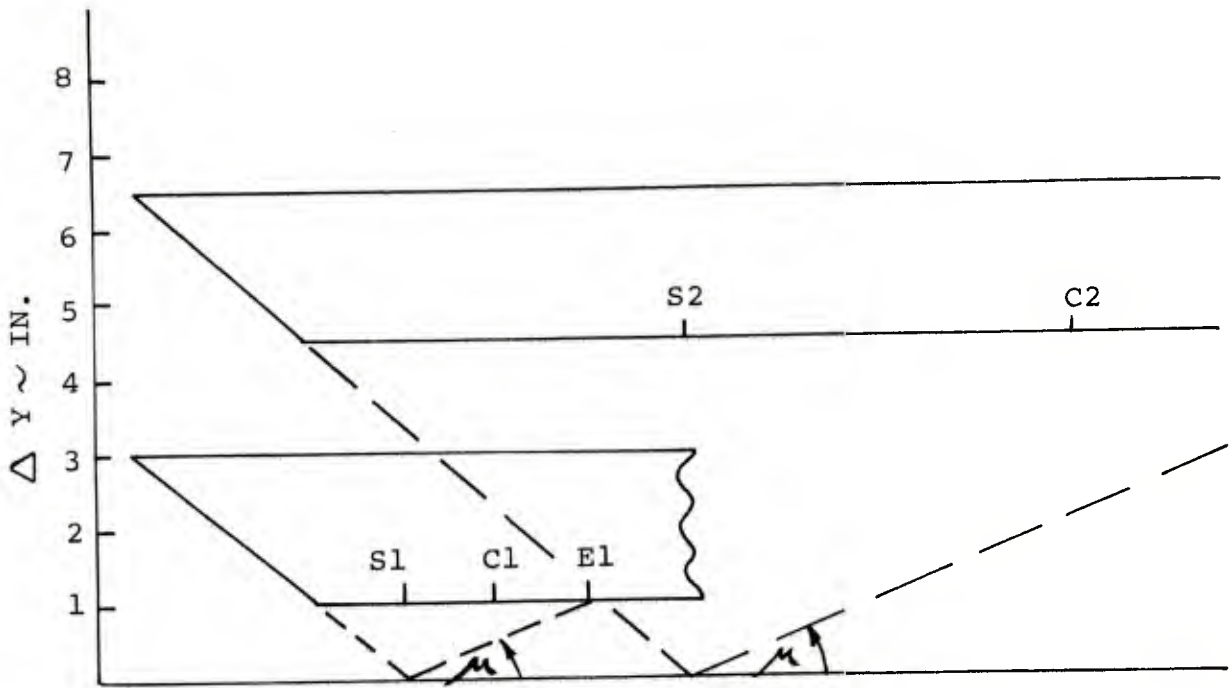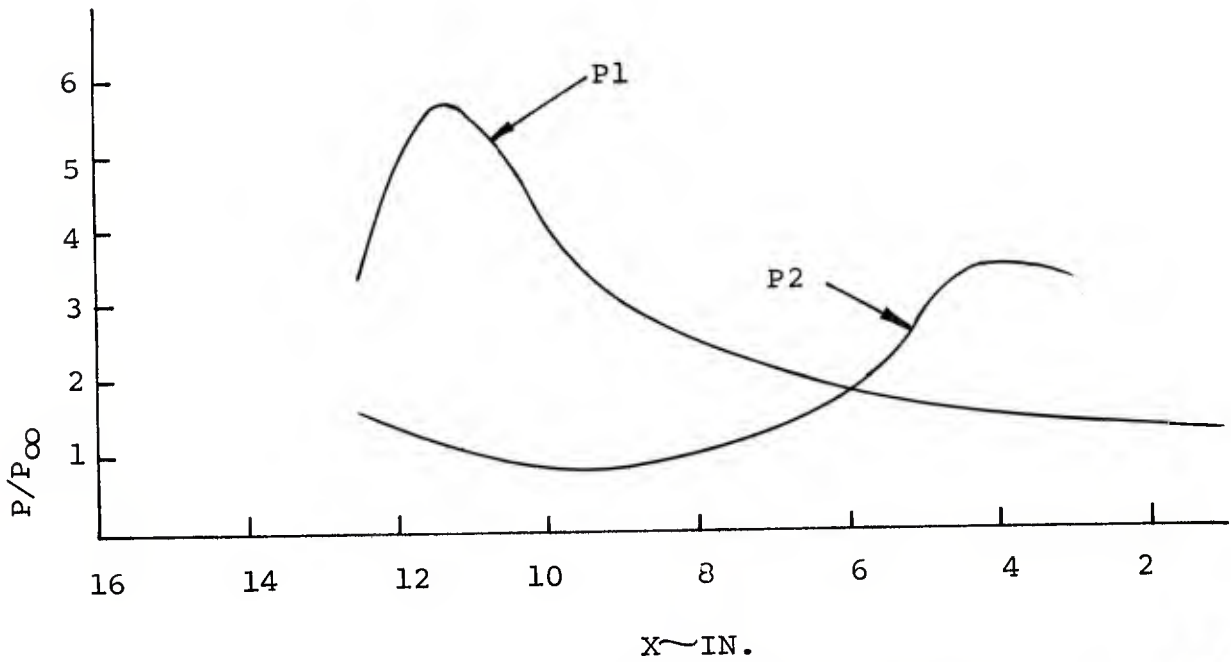
FIGURE 6 – SABOT UNDERSIDE PRESSURE PULSE GEOMETRY

The reason why this simple procedure furnishes acceptable results is not clear. One would expect the sabot bow shock to impinge on the projectile surface upstream of the point (S) determined by projection of the sabot face. Similarly, the reflected shock is stronger than the assumed Mach wave reflection. These factors would lead one to expect the intersection zone of the reflected shock wave to lie upstream of the zone presently estimated. It is conjectured that the sabot bow shock and the reflected shock resulting from impingement on the projectile surface propagate in non-uniform local flow environments produced by the sabot and projectile corner expansions which tend to translate the wave geometry rearward to a position compatible with that estimated using the simpler approximate procedure. The growth in extent of the separation region is consistent with available separated flow descriptions,[9-11] in that as ΔY increases, the shock impingement zone moves rearward, leading to larger approach boundary layer thickness and correspondingly longer separation lengths. The subsequent decay in the elevated pressure is not consistent with a flat plate shock impingement analog, however, and is conjectured to result from effects due to reflections of the two corner expansion waves and lateral venting around the sabot sides.

(4) For small separations, the data indicates that a smooth expansion occurs (see Figure 2). This change in behavior was judged to occur when the shock impingement point moves

to such close proximity with the sabot corner that a free turbulent

interaction cannot exist. In this instance, the presence

of the corner is "known" to the separation process resulting

in smoothing of the effective expansion contour. This behavior

was modeled as a Newtonian expansion about a cylindrical

effective obstacle as schematicized in Figure 7. The effective

cylinder radius is determined directly from the sabot thickness

by assuming the corner to be the sonic point, since the

sonic point on a cylinder ($\theta*$) is known from the sonic pressure

ratio for an assumed Newtonian flow. This procedure is used

whenever the previous procedure (3) would predict a pressure

pulse center which lies upstream of the point where the Newtonian

distribution falls to the separation pressure level.

(5) The fourth feature of the sabot underside pressure dis-

tribution which required modeling is the clear systematic effect of

sabot pitch angle illustrated in Figure 4. It was reasoned that

the growth of the peak pressure level, particularly at high

incidence and small lateral separation, would be caused by

convergence of the flow as the exit station is approached.

A one-dimensional flow model was developed to describe this

behavior, as schematicized in Figure 8. Expansion of the

sabot cup face flow through a Prandtl-Meyer fan results in the

background pressure level (P_1) and a corresponding Mach number (M_1).

This Mach number also corresponds to a particular value of area

ratio ($A/A*$). Using this value, a critical pitch angle

-17-

FIGURE 7 — NEWTONIAN EXPANSION PROCEDURE FOR SMALL SEPARATION

$$R_{eff} = \mathcal{T}/\text{SIN } \theta^*$$

$$P/P_{t_2} = \cos^2 \theta$$

$$\theta = \text{TAN}^{-1} \left\{ \left(\cot \theta^* - \Delta x / \mathcal{T} \right)^{-1} \right\}$$

1-1689
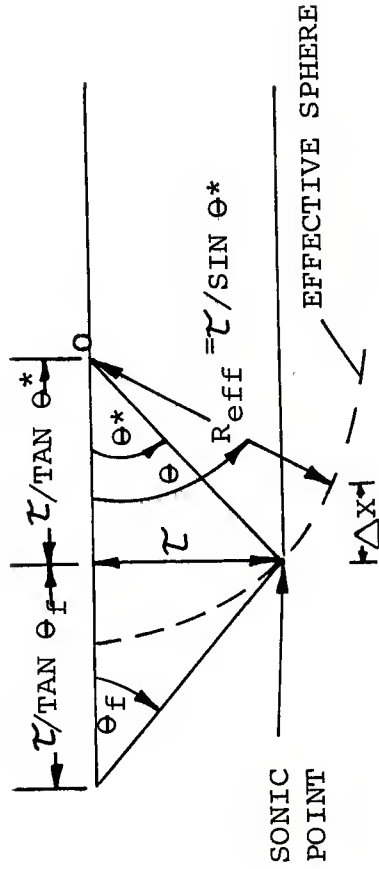
(corresponding to compression to a sonic throat at the outlet

station) can be defined. For pitch angles well in excess of this

critical angle, the location of the effective throat will occur

at a distance ($\Delta \ell$) upstream from the outlet station. Since

isentropic compression of a supersonic flow through a sonic

condition is not possible, the pressure downstream of this

"throat" has been set at a value corresponding to a normal shock

condition for the background flow at $M = M_1$. To clarify this

procedure, consider the conditions corresponding to test 190

($\Delta y = 1$ in., $\alpha = 18^\circ$). The sabot face flow is detached.

Turning this normally shocked flow through the 40° expansion

(with $\gamma = 1.4$) at the sabot corner results in a background

pressure level: $p_1/p_\infty = p_{t_2}/p_\infty \cdot p_1/p_{t_2} = 26.5 \times 0.055 = 1.5$

and a corresponding Mach number of 2.54. The area ratio (A/A*)

for a Mach 2.54 flow is 2.74. For the 13 in. sabot underside

length used in the testing (corner to outlet) the critical

pitch angle for compression to sonic conditions at the exit

station for a 1 in. lateral separation (ΔY) is:

$$\alpha_{CRIT} = \text{ARC SIN} \left\{ \frac{1}{13} \quad (2.74 - 1) \right\} = 7.7^\circ$$

This means that for test 190 the relative sabot pitch angle

was sufficiently large for choking to occur. The location of the

choking point in the assumed 1-D channel comes from simple geometry

(i.e.: where the local lateral distance (Y) is 1/2.74th of the

inlet value (Y_{IN})). For this case, this occurs 2.7 inch upstream of

$$\sin \alpha_{CRIT} = \frac{\Delta Y}{\ell}\left(\frac{A}{A^*} - 1\right)$$
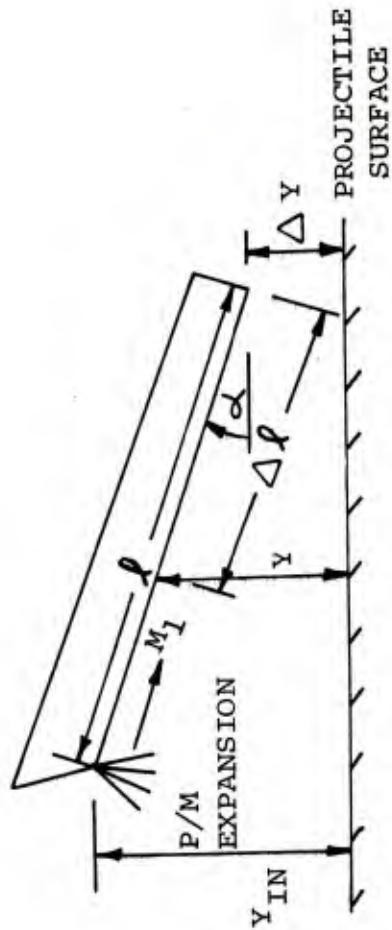
$$\frac{\Delta \ell}{\ell} = \frac{1 - \sin \alpha_{CRIT}\big/ \sin \alpha}{A/A^*}$$

$$A/A^* = f_1(M_1)$$

$$P_2/P_1 = f_2(M_1)$$

FIGURE 8 – ONE-DIMENSIONAL DUCT MODEL FOR LARGE INCIDENCE

1-1689

the outlet station. The corresponding normal shock pressure
level (at M_1 = 2.54) is:

$$P_2/P_\infty = P_2/P_1 \cdot P_1/P_\infty = 7.36 \times 1.5 = 11.$$

The complete pressure distribution is given in Figure 21.

(6) The above procedure was found to adequately predict
the level of pressure and the location of the high pressure zone
for pitch angles well in excess of the critical value. The
semi-empirical results presented in Figures 9 - 10 were then
devised to obtain a smooth variation over the intervening
pitch angle range $(0 \leq \alpha \leq 2.5 \, \alpha_{crit})$. The data presented
in Figure 9 indicates that a non-dimensional pressure function (φ)
can be defined which scales the peak pressure level between the
predicted separation pressure level at zero incidence and the
predicted normal shock pressure level for $\alpha \geq 2.5 \, \alpha_{crit}$.
Predicted pressure levels were used as the anchor points of the
correlation in order to maintain generality. The data is seen
to diverge from the fit at α = 0. This occurs because the
test data was somewhat in excess of the predicted separation
pressure. Note that this same functional form was also constructed
analytically by the following means. The separation pressure
rise for the approach flow is known from the correlation given
previously. Wedge flow tables[7] were then used to infer
the corresponding deflection angle. To clarify for the Mach
2.54 channel flow corresponding to a detached sabot bow shock,

FIGURE 9 - PEAK PRESSURE CORRELATION

$$\varphi = \dfrac{\dfrac{P/P_\infty\big|_{PEAK} - P/P_\infty\big|_{SEP}}{P/P_\infty\big|_{NS2} - P/P_\infty\big|_{SEP}}}{}$$

● DATA ▲ CALC.

$\varphi = 0.4 \ \alpha/\alpha_{CRIT}$

α/α_{CRIT}

φ

PT190

PT167

PT149

PT133

PT109

∕∕AVCO
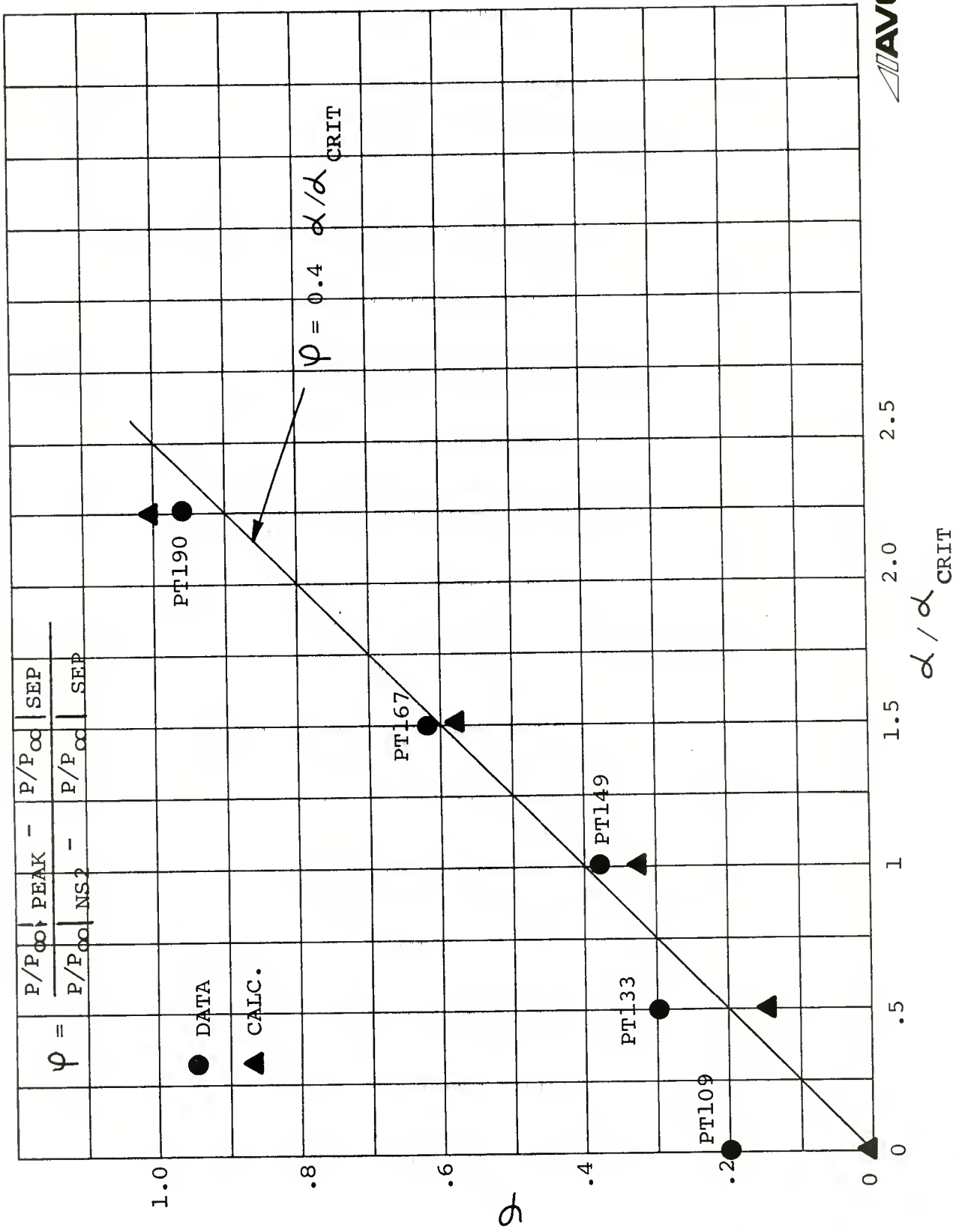
the separation pressure rise is: $p_{sep}/p_1 = 1 + (2.54 - 1)^{3/2} = 2.91$. From the wedge flow tables, an 18° deflection is required to produce this pressure rise in a Mach 2.54 flow. This deflection angle is added to the sabot angle of attack to define an effective total deflection angle and the corresponding pressure rise is computed from the wedge tables (at $M_1 = 2.54$). This simple procedure furnished pressures at incidence which exhibited good agreement with the test data behavior.

Figure 10 presents the corresponding empirical correlation for predicting the downstream migration of the peak pressure point observed in Figure 4.

(7) One additional feature exhibited by the test data (shown in Figure 4) is a tendency for the pressures downstream of the peak to remain elevated well above the background level for intermediate values of pitch angle. This effect was also modeled semi-empirically (for simplicity). It was found that these end point ($x = 0$) pressure values scaled according to the same formula as did the peak values when the predicted separation pressure value was replaced with the predicted background pressure estimate.

FIGURE 10 - LOCATION OF PEAK PRESSURE

$$\chi = \frac{x_P(\bar{\alpha}) - x_P(2.5)}{x_P(0) - x_P(2.5)}$$

$$\bar{\alpha} = \alpha / \alpha_{crit}$$

$$1 - \varphi = 1 - 0.4\alpha / \alpha_{CRIT}$$
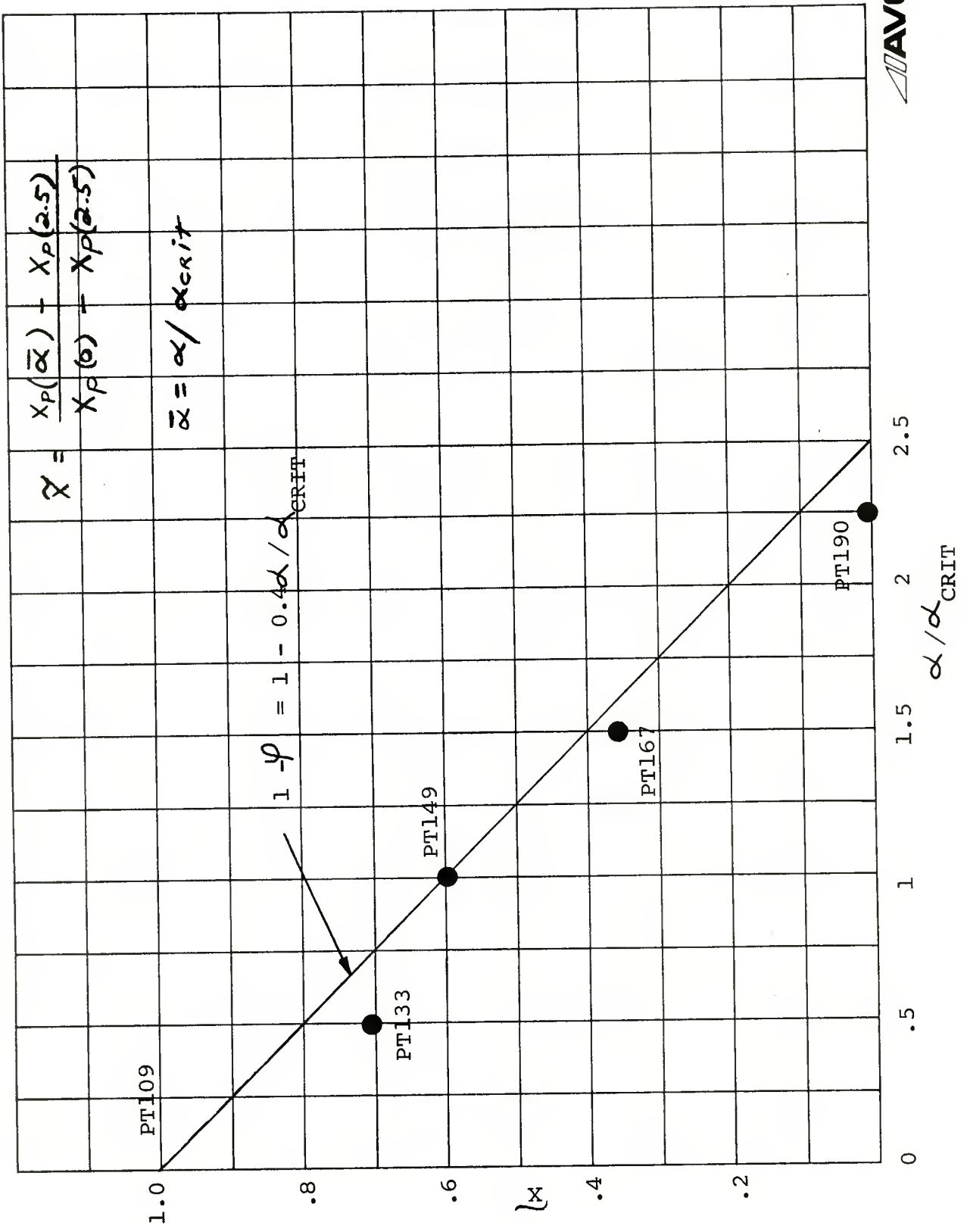
(8) Distributional shapes were developed by first using the geometry procedures of part (3) and Figure 6 to locate the start of the pressure rise region. The location of the peak pressure was then obtained by use of Figure 10. A linear increase was assumed between these two points. Downstream of the peak pressure location, a linear decrease was assumed. This decrease was terminated at a point where the pressure had fallen back to its end point value, defined in part (7). For $\alpha > 2.5 \alpha_{crit}$, the procedures of part (5) were used to define the location of the start of the constant high pressure zone. A linear variation back to the background pressure level was assumed upstream of this point.

(9) The pressure distribution on the lateral sabot edges was taken equal to the underside values as indicated by the test data and noted in comment (3) of Section 2.

(10) As for the sabot cup region, Newtonian forces were also evaluated and are applied in any case where the Newtonian force exceeds that predicted from the interaction model.

3.3 PROJECTILE PRESSURE MODEL

Modeling of pressures along the projectile surface

also employs local flow elements similar in nature to those described above in regard to the sabot underside.

(1) The conical projectile nosetip pressures are evaluated using the modified Newtonian approximation.[8] This value is somewhat below that predicted using conical flow tables.[7] However, unless the sabot shock lies forward enough to produce interaction on the conical tip section, this section is in free flight and no incremental force is required in the dynamics formulation.

(2) The background pressure level and Mach number on the cylindrical surface of the projectile are taken as their ambient values. This approximation is in close agreement with values obtained by performing a Prandtl-Meyer expansion of the conical nosetip flow about the projectile's shoulder. It should also be noted that near field projectile incidences during the interaction phase are sufficiently small to allow this assumption to be generally valid.

(3) The pressure peak evident in Figures 2 -3 is presumed due to impingement of the sabot petal bow shock upon the projectile surface. Although the interaction flow field involves a series of intersections with various other compression and expansion waves before this impingement,[3-6] this flow feature has been approximated by computing the bow wave about a free flying sphere-cylinder using a numerical flow field code.[12 - 13] Results were generated for a Mach

number of 4.5, which corresponds to the test condition and also lies at about the center of the regime of interest for penetration round studies. These results, shown in Figure 11, were then curve fit for ease of computation, which is performed as follows. First, the sabot displacement and rotation are used to compute the lateral distance at which impingement occurs (y/r). The axial location (z/R) and shock strength (θ_s) are then computed from the curve fit shock solution. In performing this calculation, the effective sphere radius is defined as in Figure 7 and the origin of the axial coordinate (z) is shifted forward so that the bow shock originates at the sabot petal tip. The peak pressure level is computed by reflecting this approximate sabot bow shock wave off of the projectile surface as shown in Figure 12. For $\theta_s \geq \theta_s|_{max}$ the peak pressure is equated to a maximum value equal to the normal shock static value. Note that as y/R increases, the shock impingement point moves downstream and the shock strength decreases. This is exactly the behavior exhibited by the test results shown in Figures 2 - 3. Rotation (pitch-up) acts in a similar manner (see Fig. 5) since the origin of the sabot bow shock is also displaced laterally by this type of motion. Interaction ends as the impinging shock angle approaches the Mach angle.

(4) In the case where the sabot cup shock is attached

FIGURE 11 - SABOT BOW SHOCK BEHAVIOR
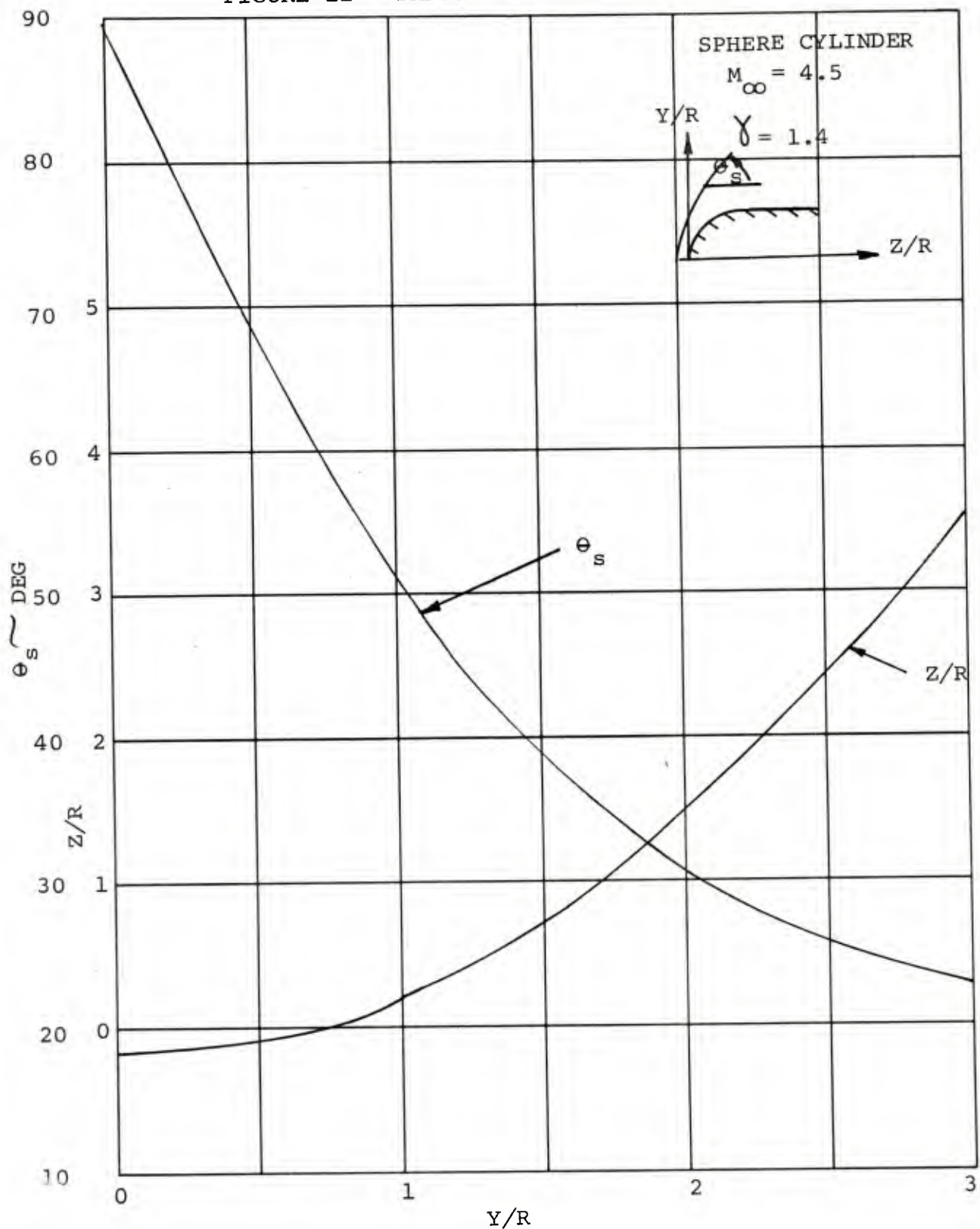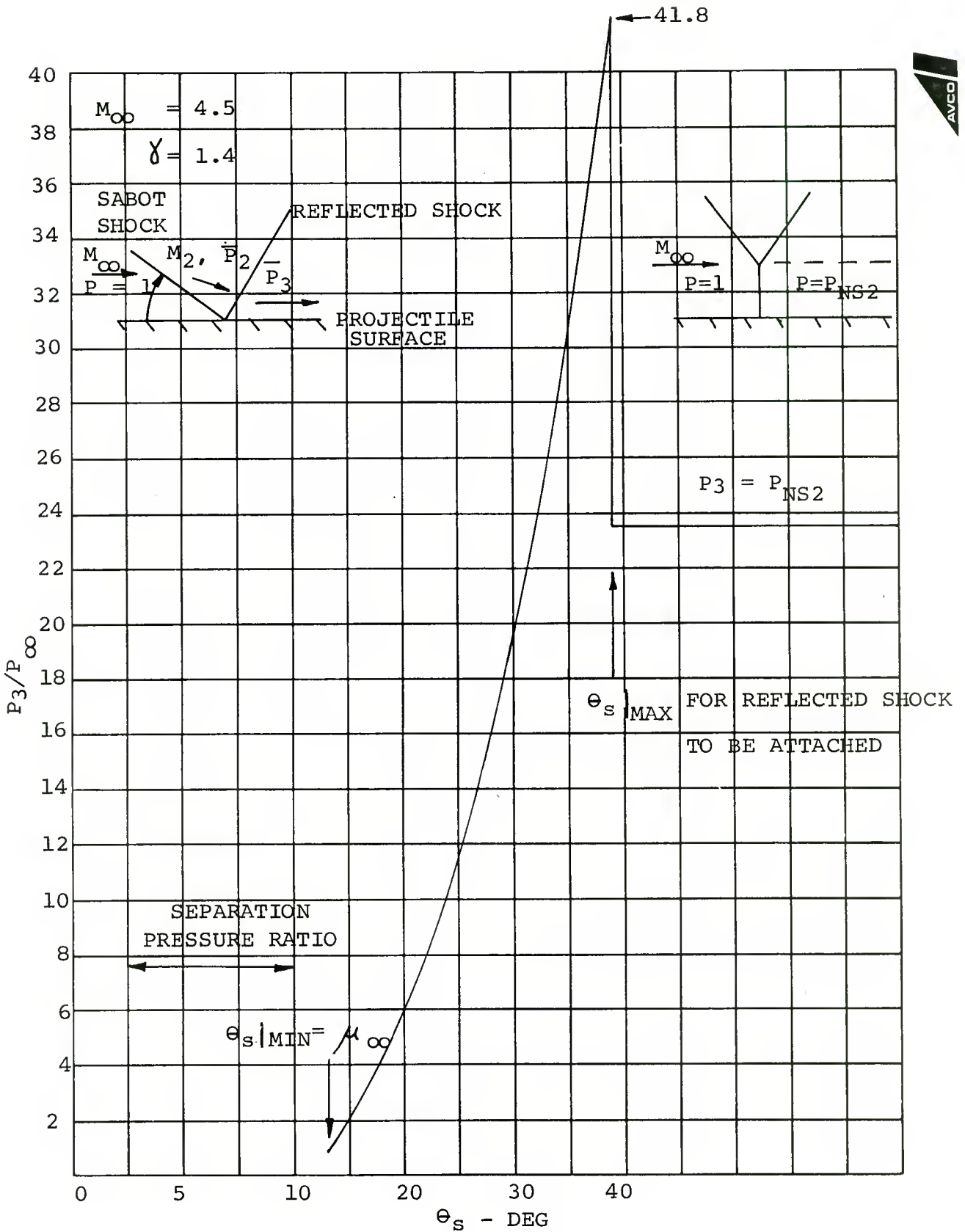
FIGURE 12 - PEAK PROJECTILE PRESSURE

(Section 3.1, part (2)) an additional translation of the shock solution is performed in order to "line-up" the curved shock with the known oblique shock[7] at the sabot underside plane $(y = t)$.

(5)   Upstream of the peak pressure bump there is a region of elevated pressure clearly evident in Figures 2, 3 and 5. This zone is assumed to be produced by boundary layer separation occurring ahead of the impinging sabot bow shock. The separation data[9] discussed previously was also used to estimate this value (see Section 3.2, part (2)). The test data indicates that the magnitude of this "precursor" pressure rise should scale roughly in proportion to the subsequently peak pressure level:

$$P_{sep} / (P_{sep})_{ref} = P_{peak} / P_{t_2}$$

$$\text{for} \quad P_{peak} > (P_{sep})_{ref} = \left\{ 1 + (M_1 - 1)^{3/2} \right\} P_{\infty}$$

(6)   The pressure data indicates that a second zone of high pressure is formed on the projectile surface near the outlet station as the pitch angle is increased. This region is produced by the same throttling process discussed in regard to the sabot underside (Section 3.2, parts (5)-(7)). Comparison of the data in Figures 4 -5 indicates that these outlet region sabot underside and projectile surface pressures

are essentially identical, implying a one dimensional flow

behavior. This pressure rise can be modeled by the same

semi-empirical procedures used on the sabot underside:

$$\frac{P_{end} - P_{\infty}}{P_{NS_2} - P_{\infty}} = 0.6 \quad \alpha/\alpha_{crit}$$

for $P_{end} < P_{NS_2}$

This equation predicts a somewhat more rapid rise (with

respect to pitch angle) of the outlet region projectile sur-

face pressure than that used on the sabot underside. This

may result because the sabot data set terminates (at $x = 3$ in.)

somewhat upstream of the projectile surface data set (at $x = 1$ in.).

   (7) The last feature of the projectile surface pressure

which requires description is the shape of the distribution.

The location of the peak (bump) is determined from the shock

impingement geometry discussed in part (3). The peak pres-

sure (bump region) distribution was taken as triangular in

shape, centered at the above defined impingement point,

and with a width equal to the sabot underside's

(zero incidence) pulse width defined in Section 3.2, part (3).

Note from the data in Figure 5 that the projectile surface

pressure pulse width appears to be essentially independent

of incidence angle. The region of separated flow appears to wet

the entire cylindrical surface of the projectile as long as

the peak (bump) pressure ratio exceeds the critical value for

separation as indicated in part (5). When the peak (bump) pressure ratio falls below this critical value, there is no longer an additional zone of elevated pressure ahead of the shock impingement zone.

Figure 13 presents a summary overview of the flow field model which highlights essentially all of the local flow elements used to describe the overall surface pressure/aerodynamic force behavior. The numbers in the parentheses indicate the sections of the text in which the details of each indicated flow element model can be found.
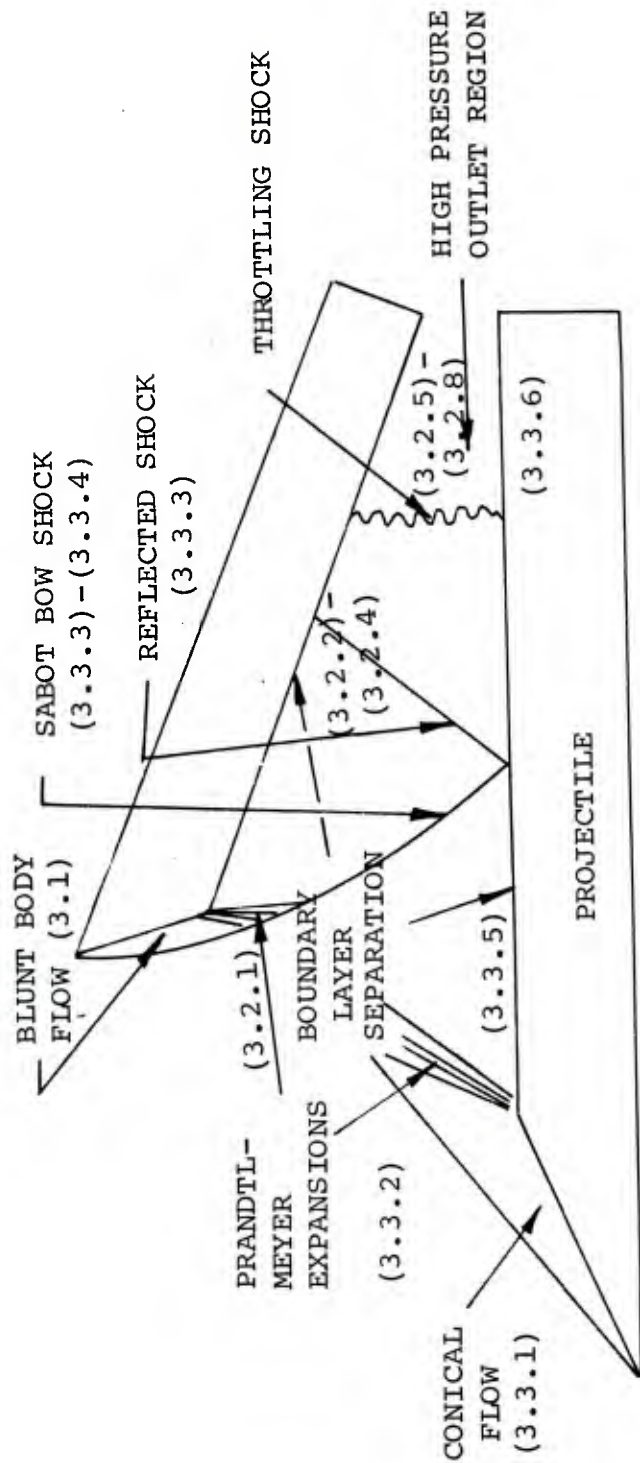
FIGURE 13 - OVERVIEW OF FLOW FIELD MODEL

BLUNT BODY FLOW (3.1)

SABOT BOW SHOCK (3.3.3)-(3.3.4)

REFLECTED SHOCK (3.3.3)

THROTTLING SHOCK

HIGH PRESSURE OUTLET REGION

PRANDTL-MEYER EXPANSIONS (3.3.2)

(3.2.1)

BOUNDARY LAYER SEPARATION

(3.2.2)-(3.2.4)

(3.2.5)-(3.2.8)

(3.3.6)

CONICAL FLOW (3.3.1)

(3.3.5)

PROJECTILE

AVCO

4.0 <u>RESULTS</u>

In order to further clarify this engineering modeling
of the interaction flow field, a series of comparisons with
the experimental test data will be presented. Subsequently,
a series of dynamic motion computations for the round previously
studied[1] will be presented in order to assess the effect of
this modification of the interaction flow field upon the predicted
component dynamics.

4.1 COMPARISON TO WIND TUNNEL DATA

Figures 14 - 16 present comparisons of the predicted sabot
pressures with the BRL test data[2] for cases at zero incidence.
The results shown in Figure 14 correspond to the minimum
separation investigated experimentally. For this case, the gap
is predicted to be choked (see Section 3.1, part (3)) and
the sabot cup pressures are evaluated as on an effectively
blunt obstacle. This results in some overprediction of the
cup forces for this case, where a non-monotonic behavior of the
cup pressure is present. The pressures on the sabot underside
were computed by the procedures of Section 3.2, part (4) for
this case. Some underprediction of the test data is evident.

Figure 15 presents a comparison at an intermediate separa-
tion ($\triangle y = 1$ in.). Here the model predicts the gap to be
unchoked and the sabot cup shock to be (just barely) attached
(Section 3.1, part (2)). The data indicates that a detached

-35-
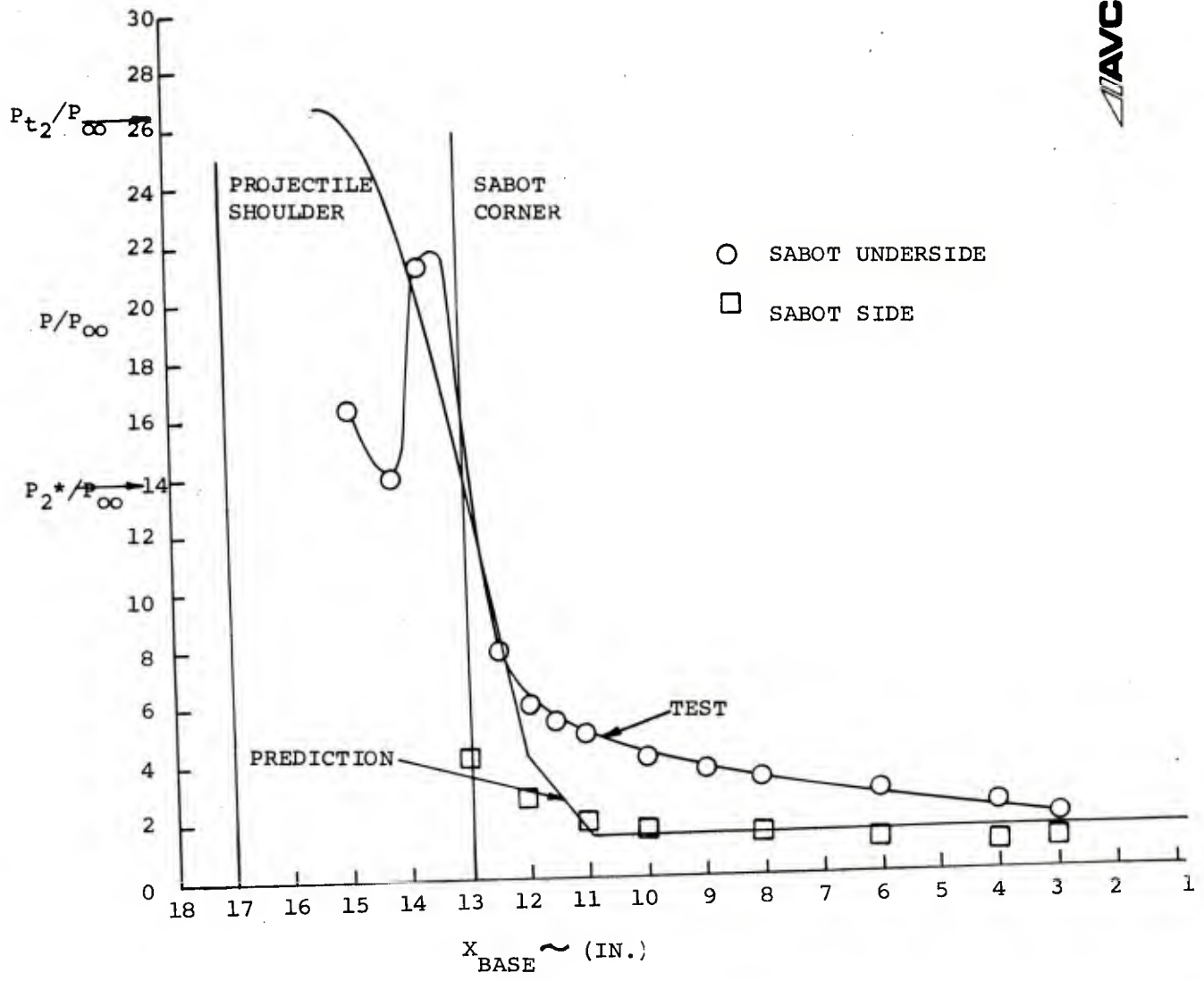
FIGURE 14 - COMPARISON OF PREDICTED AND EXPERIMENTAL SABOT PRESSURE FOR PT107, $\triangle$ Y = 0.128", α = 0°
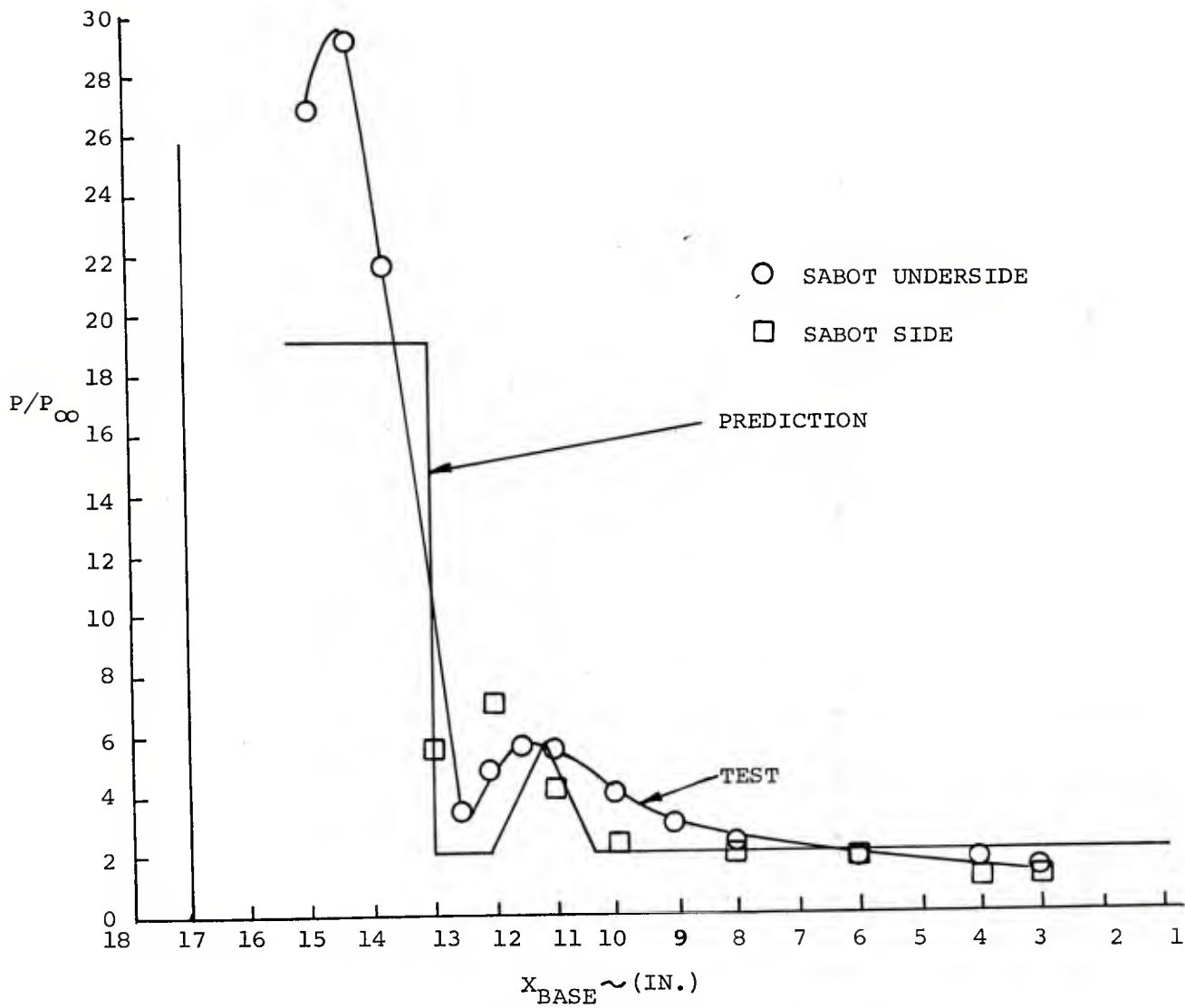
FIGURE 15 – COMPARISON OF PREDICTED AND EXPERIMENTAL
SABOT PRESSURES FOR PT109, $\Delta Y = 1"$, $\alpha = 0°$

-37-

structure existed. This discrepancy could be due to a number of causes: (1) the sabot leading edge must have some finite radius of curvature; (2) there is a boundary layer (displacement effect) on the sabot face which has not been considered in the modeling; and (3) the sabot bow shock suffers interactions with the projectile shock which have also been neglected. However, since the average cup pressure is reasonably approximated and since this situation of moderate separation without incidence is not likely to occur during actual discards, no further refinement of the model was pursued in this area. The sabot underside pressures for this case were estimated using the procedures of Section 3.2, parts (1) - (3). Note that a shift in the background pressure level has occurred between this case and the previous case. This has resulted primarily from the different stagnation pressures for the sabot cup flow, since the initial Mach numbers for the Prandtl-Meyer expansion[7] around the corner between the face and sabot underside is effectively unity in both cases.

Figure 16 presents a similar comparison at the largest value of separation tested at zero incidence. The sabot cup shock is still predicted to be attached. Here the sabot underside pressures are somewhat overpredicted. This again results primarily from the higher background pressure level predicted by the attached shock condition.
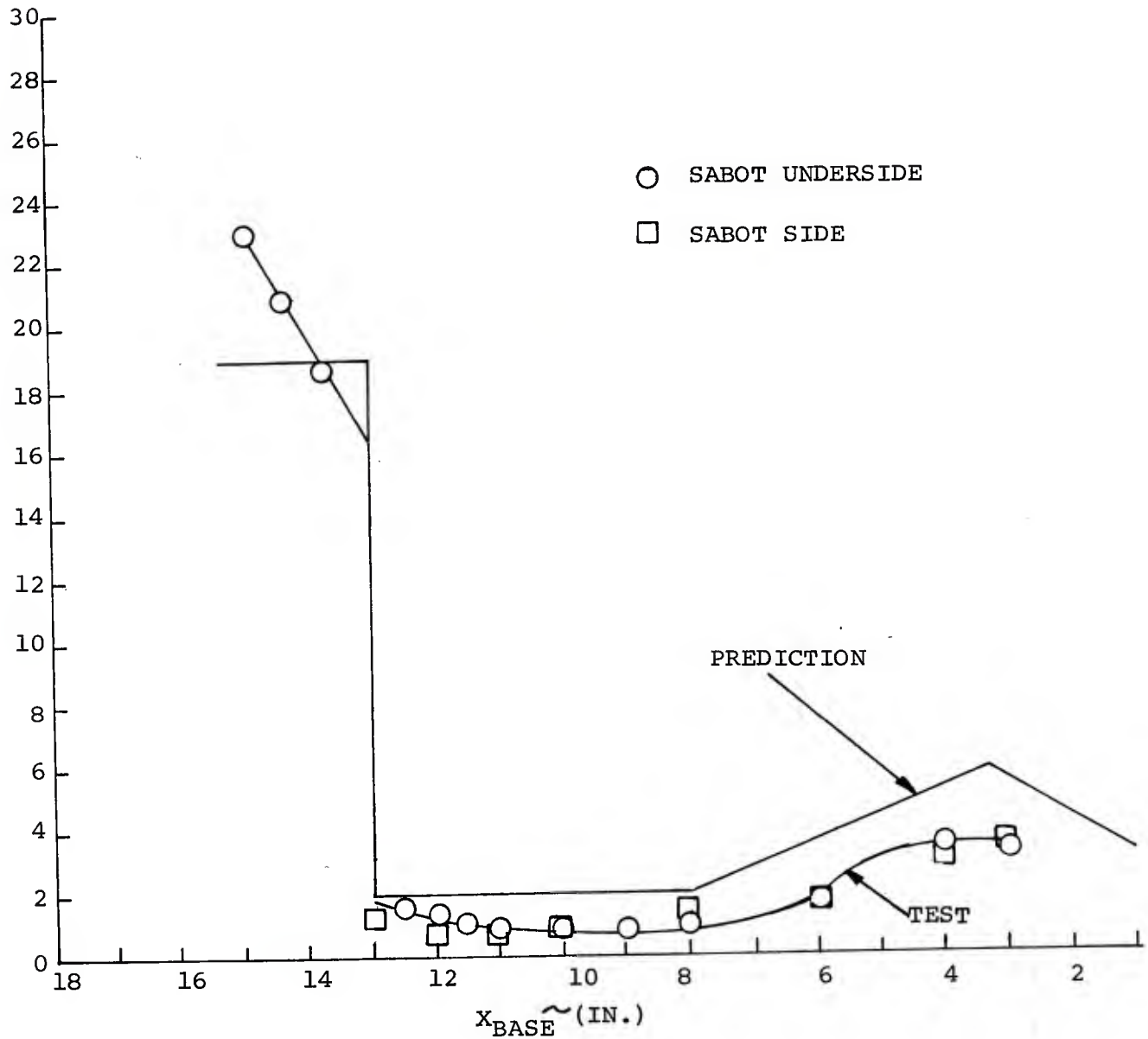
FIGURE 16 - COMPARISON OF PREDICTED AND EXPERIMENTAL
SABOT PRESSURES FOR PT116, $\Delta y = 4.5"$, $\alpha = 0°$

Figures 17 - 20 present comparisons of the predicted
sabot pressures with the BRL test data[2] as the separation
distance is varied for an intermediate value of the pitch
angle. Here the sabot bow shock is predicted to be detached
in all cases due to the effect of the pitch angle. For a
fixed angle of attack, the critical angle (α_{crit}) for
throttling down the gap flow decreases with decreasing
separation (see Section 3.2, part (5)). Thus, the behavior
of the sabot underside pressure distribution approaches the
zero incidence asymptote as $\triangle y$ increases for fixed incidence.
Conversely, more effects of flow constriction are evident
as separation distance decreases for fixed incidence.

Figures 21 - 24 present similar comparisons of predicted
sabot pressures with BRL test data[2] as the separation distance
is varied for the largest angle of attack tested. Here
we see that there is no separation pressure bump predicted
for the larger separation cases. This has resulted because
the sabot bow shock was found to miss impinging upon the
projectile surface (see Section 3.2, part (3) and Figures 34 -35).

In all these Figures the sabot lateral edge pressures have
also been given in order to demonstrate the essential equality
of the lateral side sabot pressure distribution to that
along the sabot underside centerline.
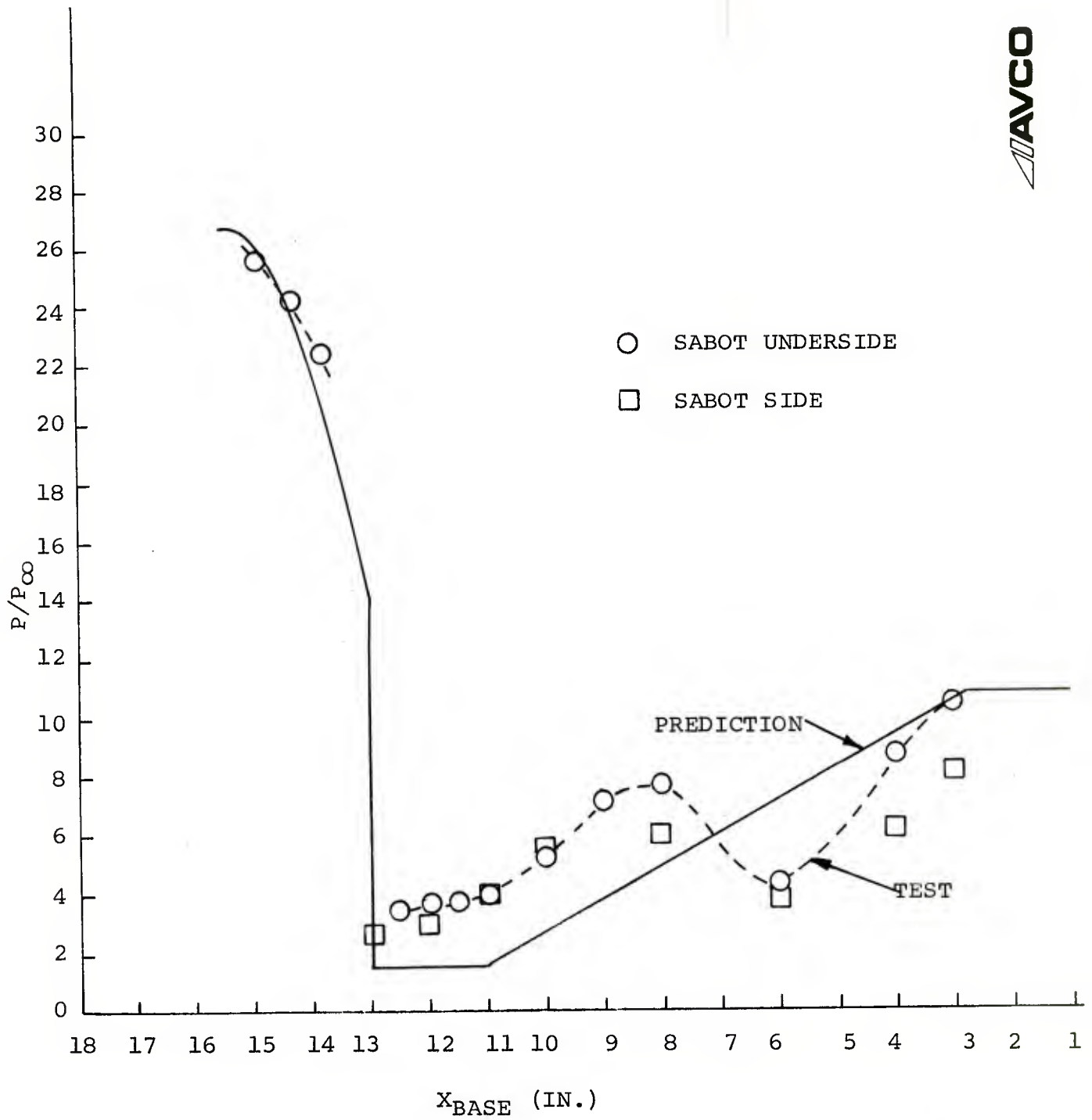
FIGURE 17 – COMPARISON OF PREDICTED AND EXPERIMENTAL SABOT PRESSURES FOR PT150, $\Delta_Y = 0.5"$, $\alpha = 8^\circ$
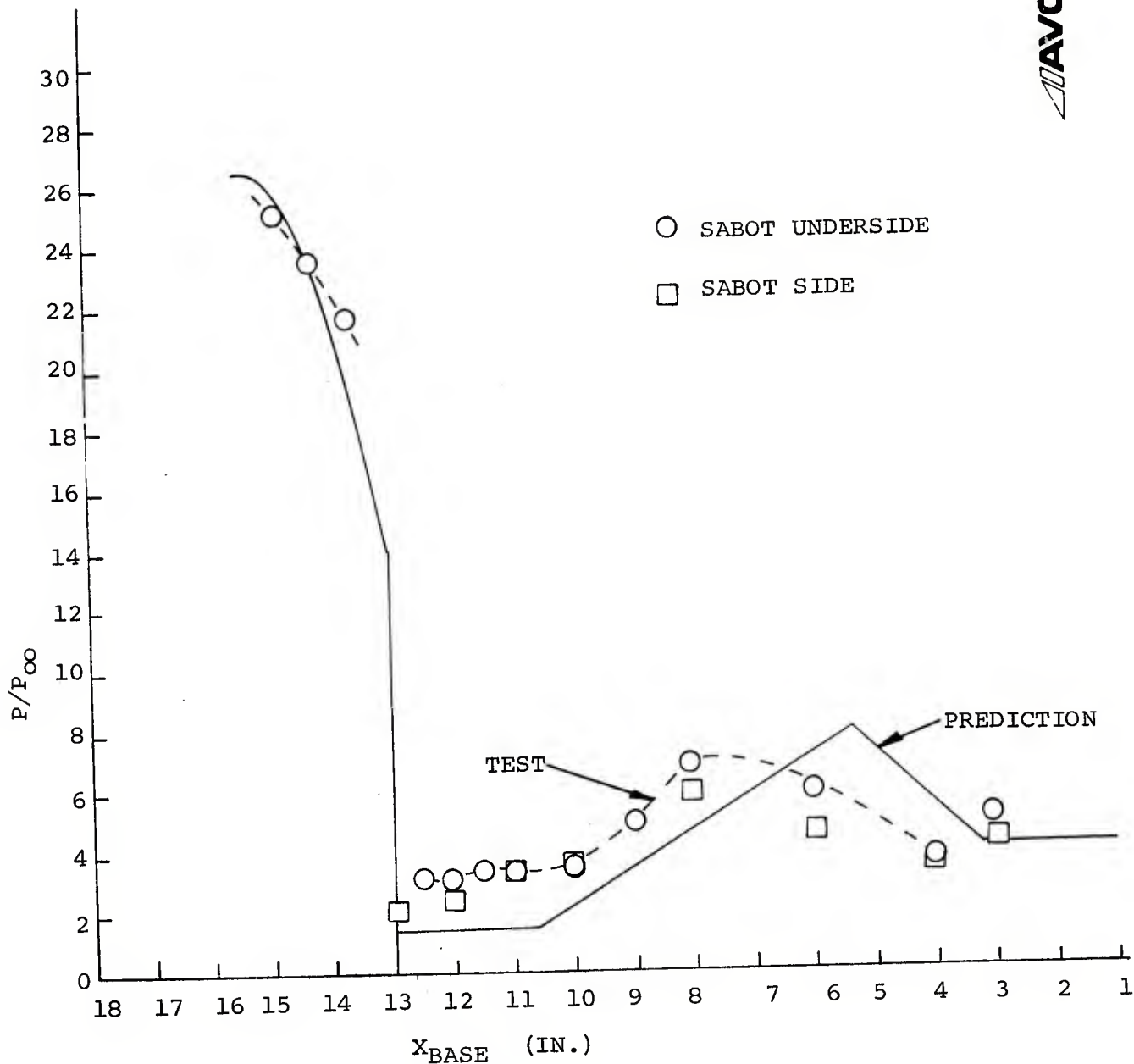
FIGURE 18 - COMPARISON OF PREDICTED AND EXPERIMENTAL SABOT
PRESSURES FOR PT149, $\triangle Y = 1.0"$, $\alpha = 8^{\circ}$
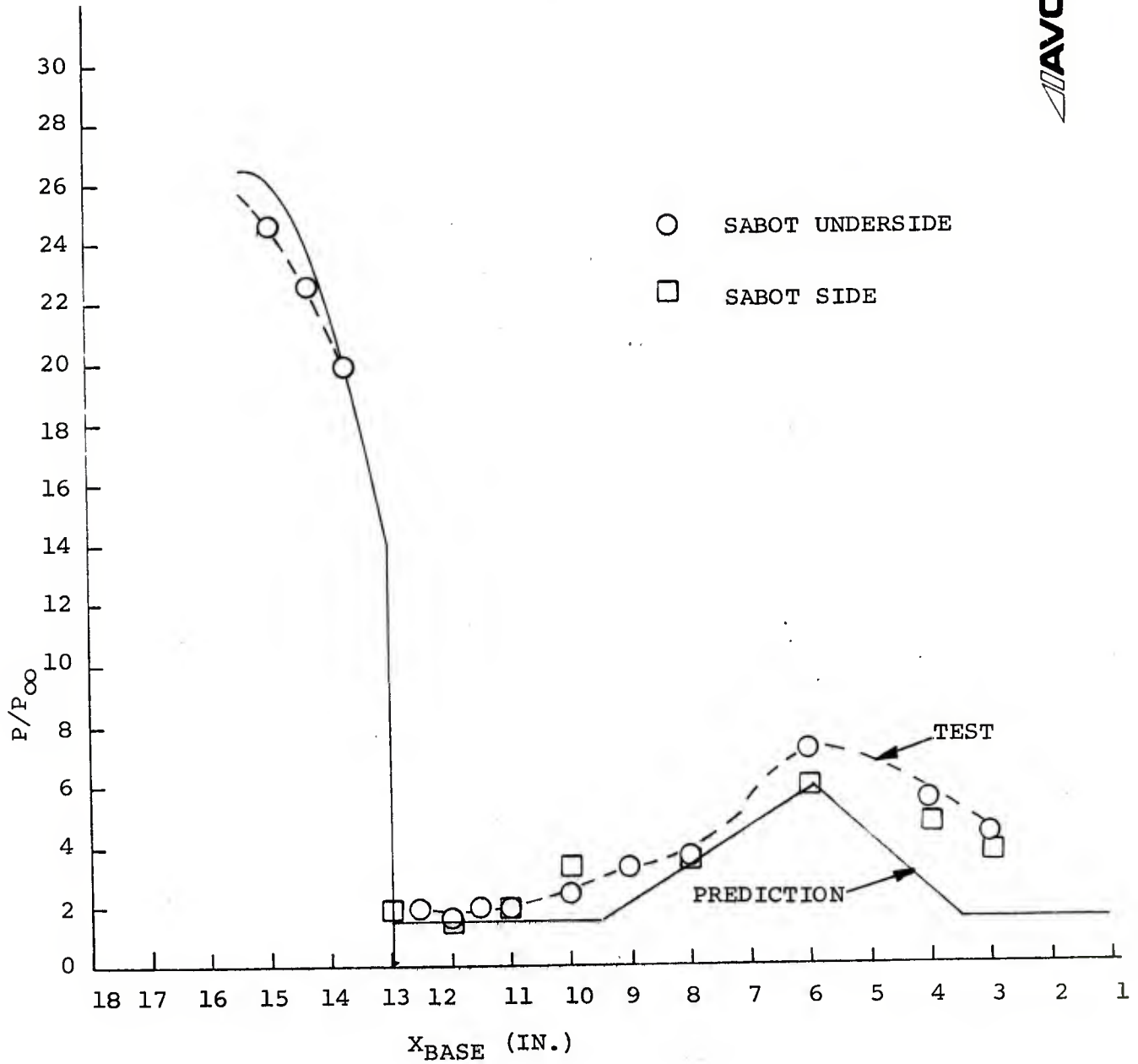
FIGURE 19 – COMPARISON OF PREDICTED AND EXPERIMENTAL SABOT
PRESSURES FOR PT147, $\triangle Y = 2.0"$, $\alpha = 8°$

AVCO

30
28
26
24
22
20
18
16
14
12
10
8
6
4
2
0

P/P_∞

○ SABOT UNDERSIDE

□ SABOT SIDE

PREDICTION

TEST

18 17 16 15 14 13 12 11 10 9 8 7 6 5 4 3 2 1

X_{BASE} (IN.)
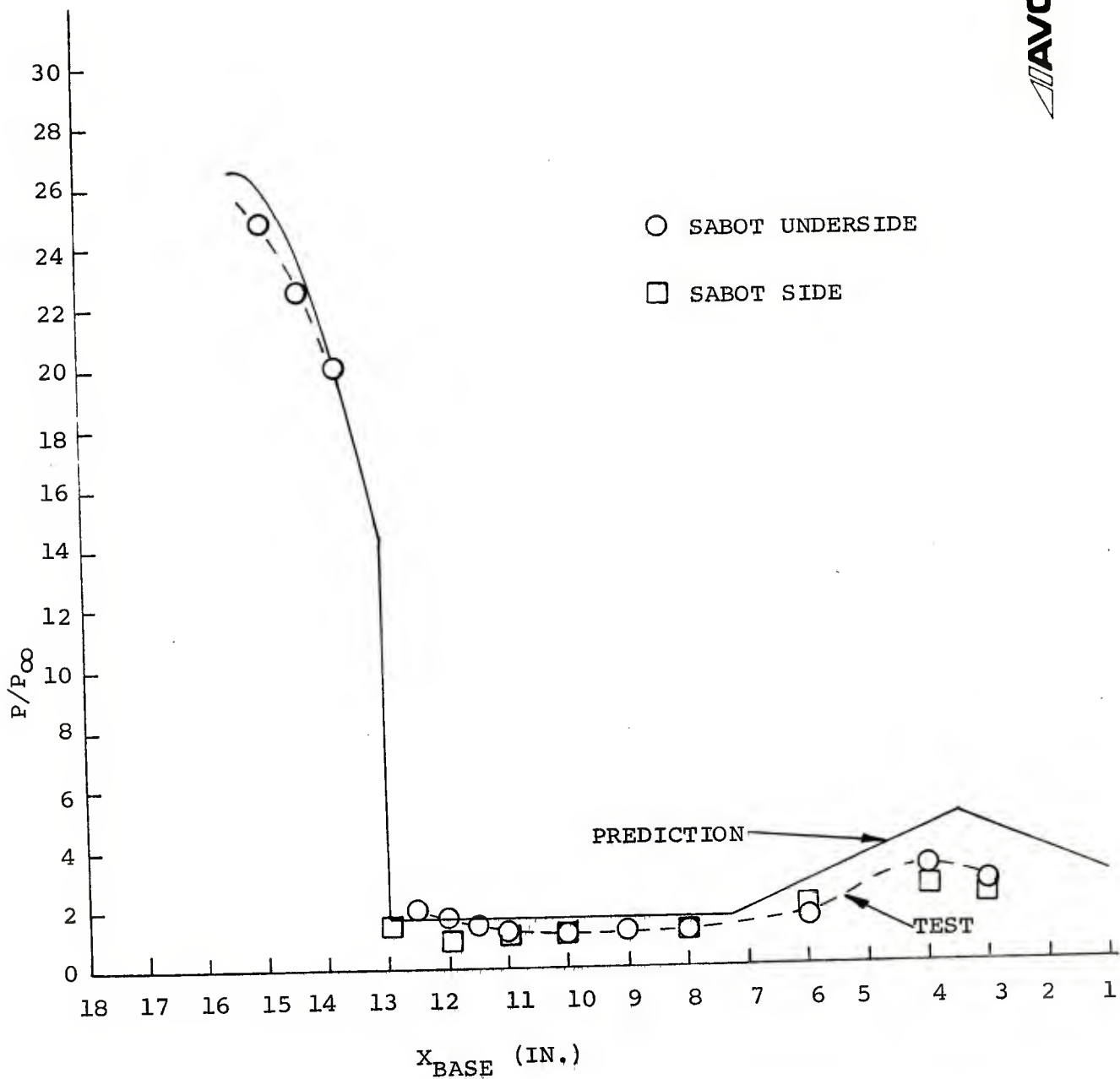
FIGURE 20 - COMPARISON OF PREDICTED AND EXPERIMENTAL SABOT
PRESSURES FOR PT145, $\triangle Y = 4.0"$, $\alpha = 8^\circ$

FIGURE 21 - COMPARISON OF PREDICTED AND EXPERIMENTAL SABOT PRESSURES FOR PT190, $\Delta y = 1"$, $\lambda = 18°$
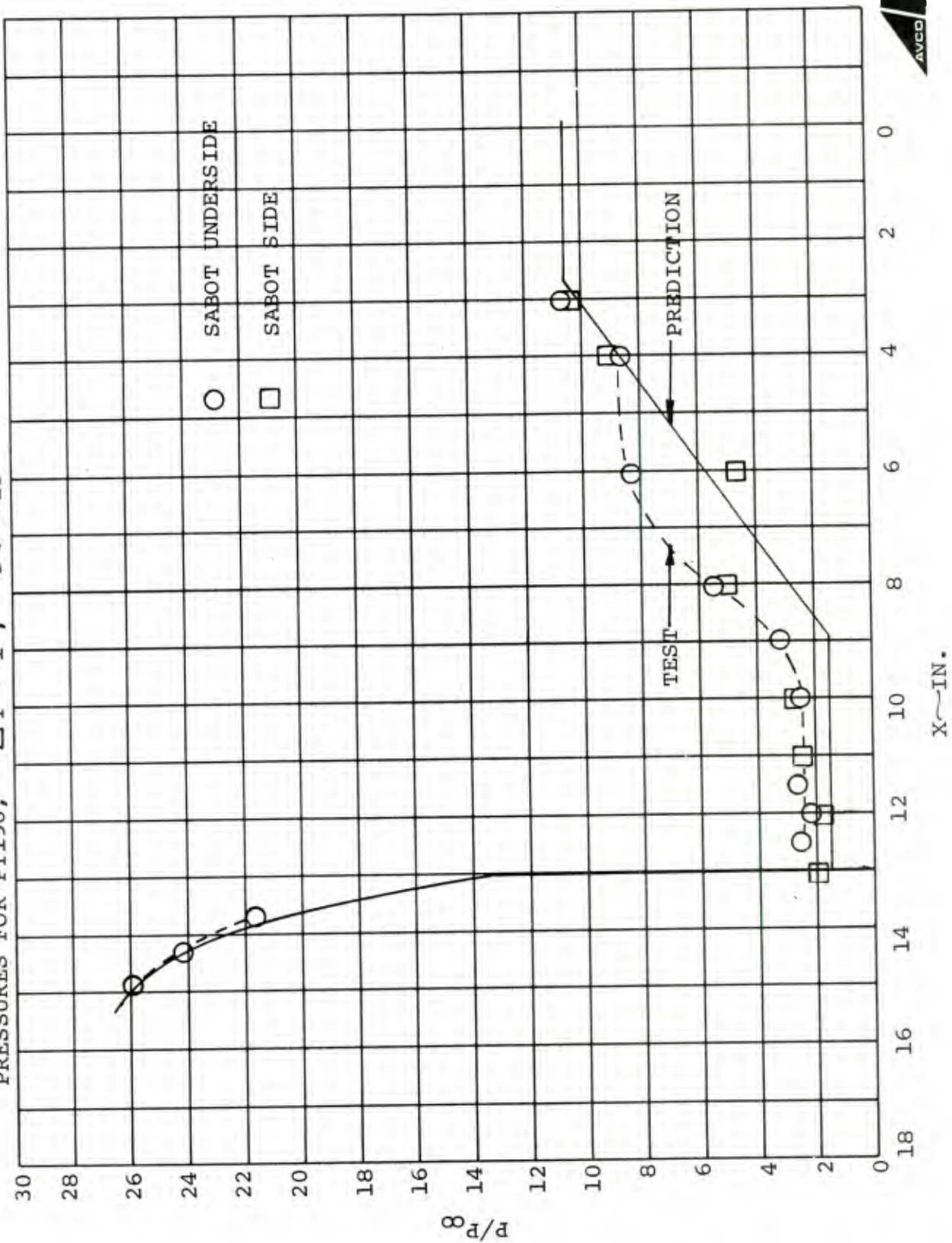
FIGURE 22 - COMPARISON OF PREDICTED AND EXPERIMENTAL SABOT PRESSURES FOR PT188, $\Delta Y = 2"$, $\alpha = 18°$
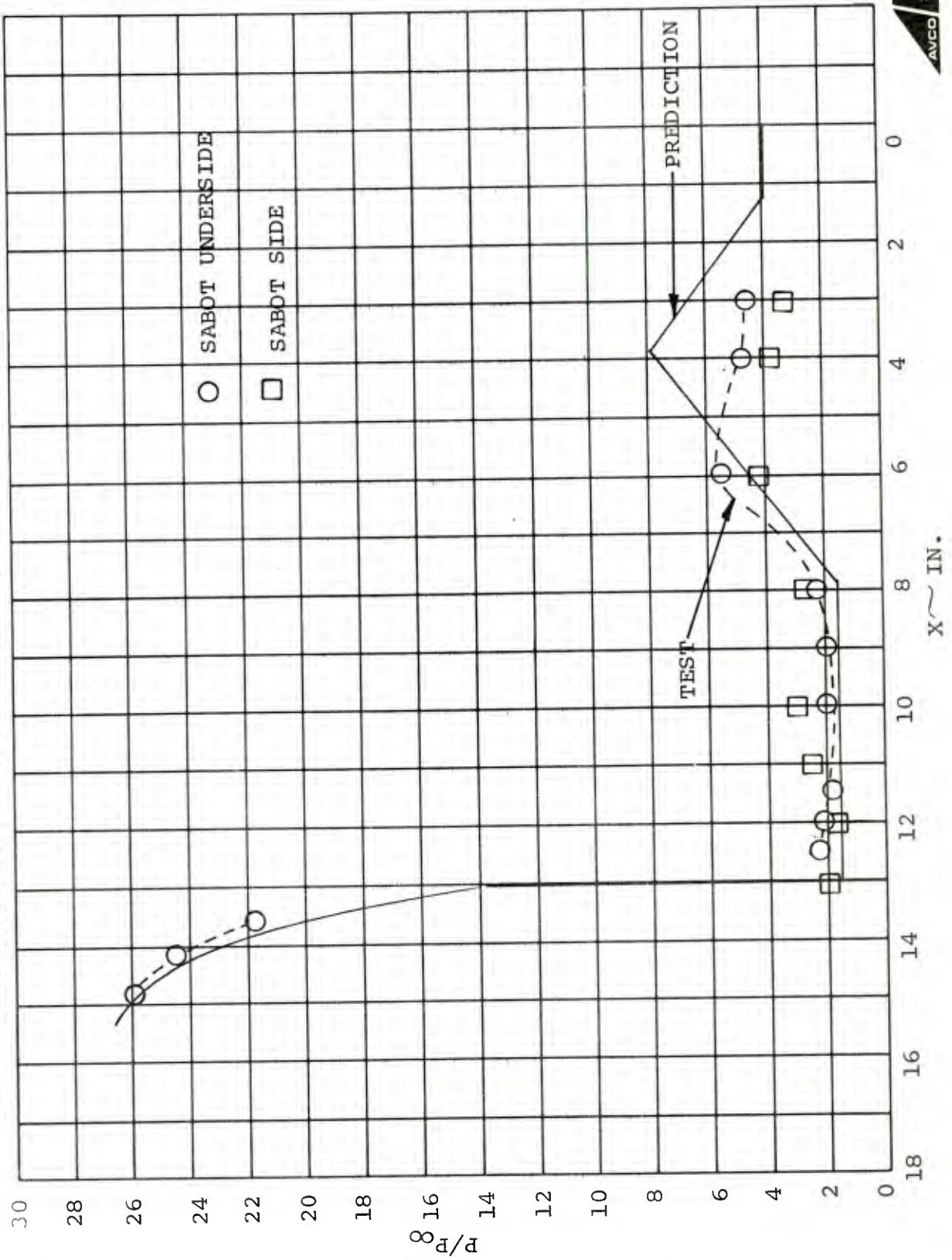
FIGURE 23 - COMPARISON OF PREDICTED AND EXPERIMENTAL SABOT PRESSURES FOR PT186, $\Delta Y = 4"$, $\alpha = 18°$
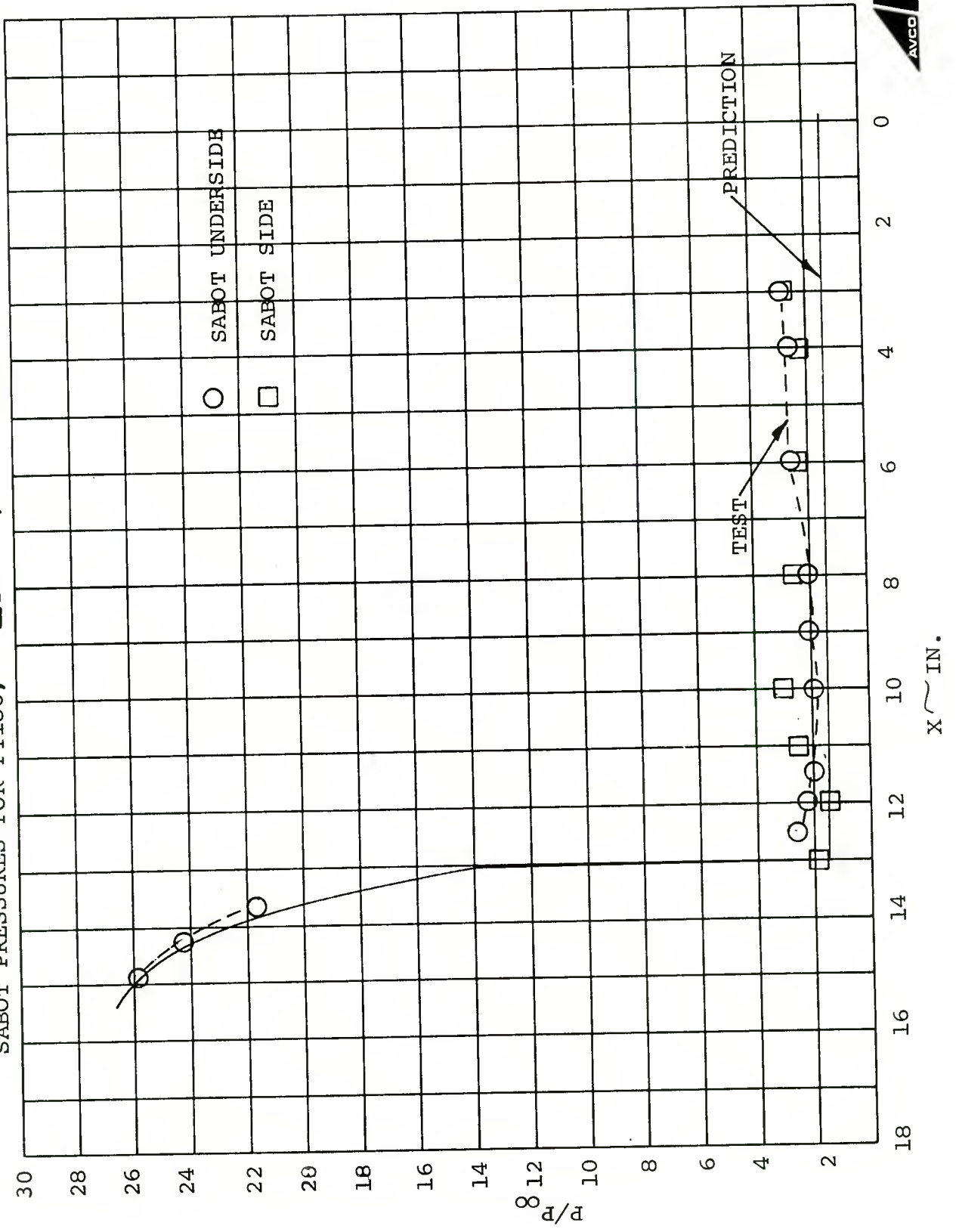
FIGURE 24 - COMPARISON OF PREDICTED AND EXPERIMENTAL

SABOT PRESSURES FOR PT 184, $\Delta y = 6"$, $\alpha = 18°$

-48-
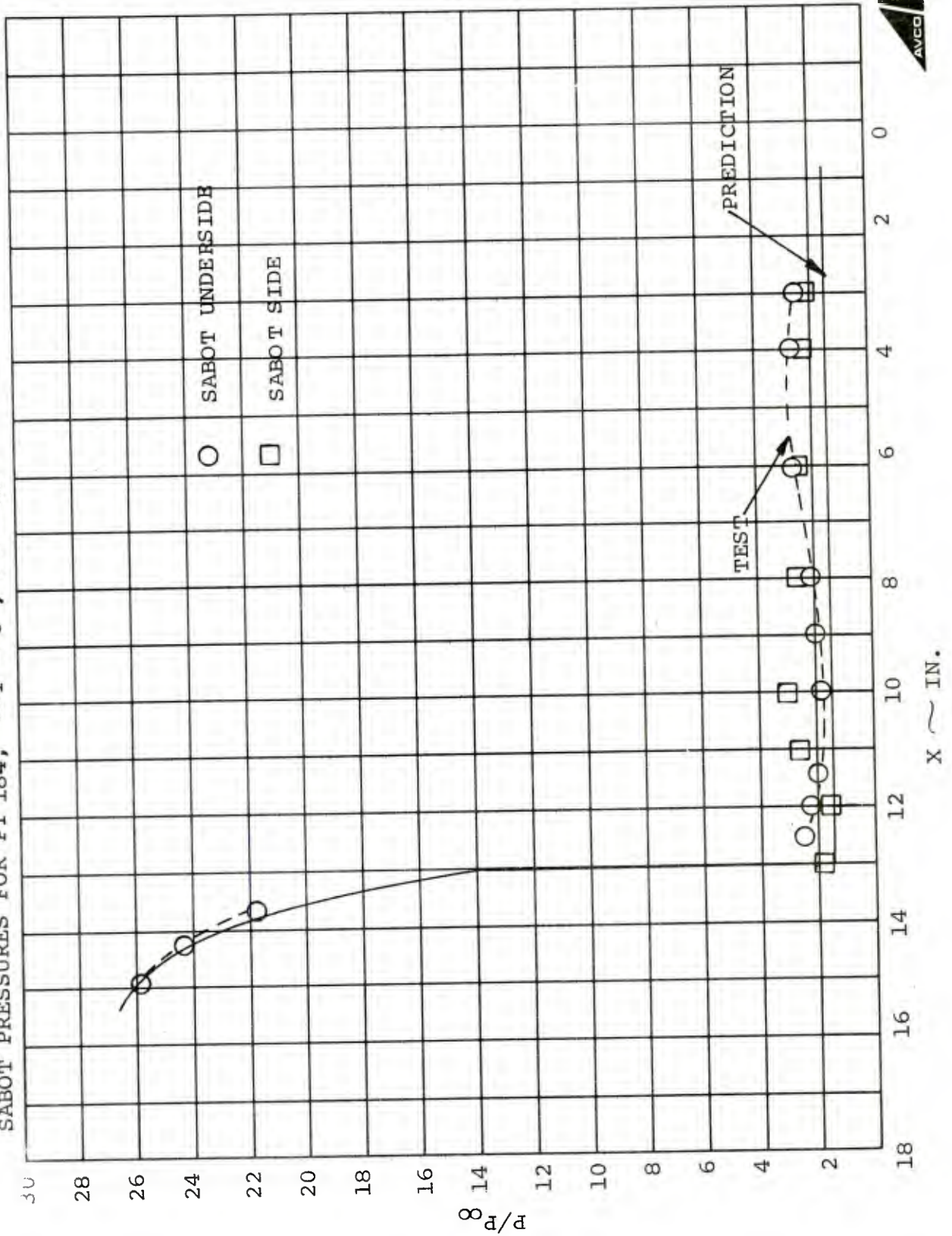
Figures 25 - 27 present the projectile surface pressure comparisons for the zero incidence cases presented previously ($\Delta y = 0.128$, 1.0 and 4.5 in.). For the smaller separation distances, the shock wave impingement angle was found to exceed its critical value to allow oblique shock reflection (Section 3.3, part (3)). The static pressure behind a normal shock was therefore imposed. For the largest separation distance case, an acceptable reflected shock solution of somewhat weaker strength has been found. There seems to be a tendency to underpredict the peak pressure level while overestimating the position for the smaller separations. For larger separations the peak is overpredicted, but the position is underpredicted. The net result should be an adequate estimate of the pitching moment over the entire range of separation distances.

Figures 28 - 31 present the comparisons for the intermediate angle of attack situation. Reflected shock solutions have been found for all cases. Note that the peak pressure for the half inch separation case is very close to the maximum possible value (see Figure 12). Here the tendency to overpredict pressure level and underpredict location at larger separations is also evident. The use of a pressure cut-off or maximum equal to the normal shock static pressure would provide somewhat better agreement for the smaller separations. This arbitrary cut-off was not imposed since the test data
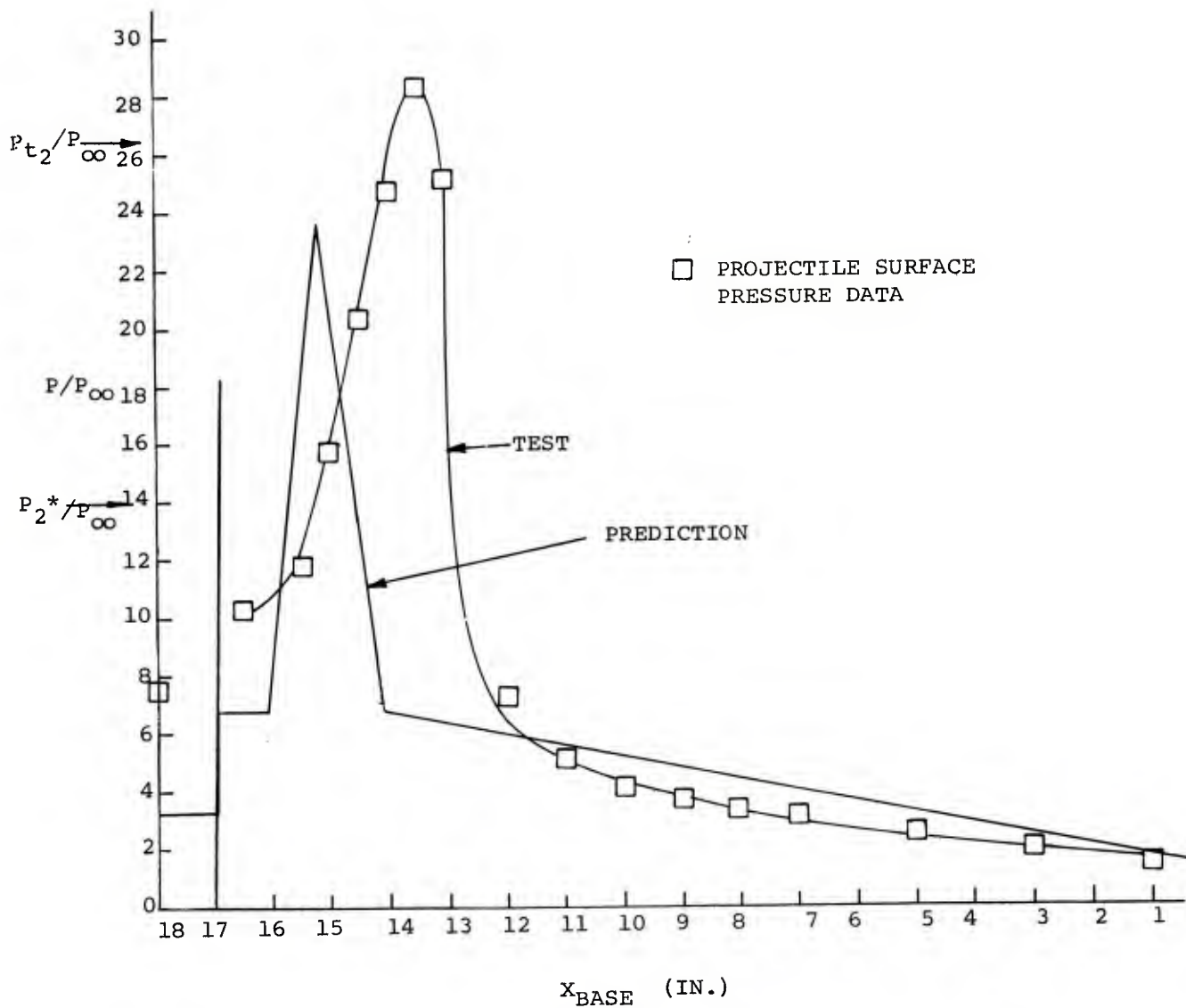
FIGURE 25 - COMPARISON OF PREDICTED AND EXPERIMENTAL
PROJECTILE PRESSURES FOR PT107, $\triangle Y = 0.128"$, $\alpha = 0^{\circ}$

-50-
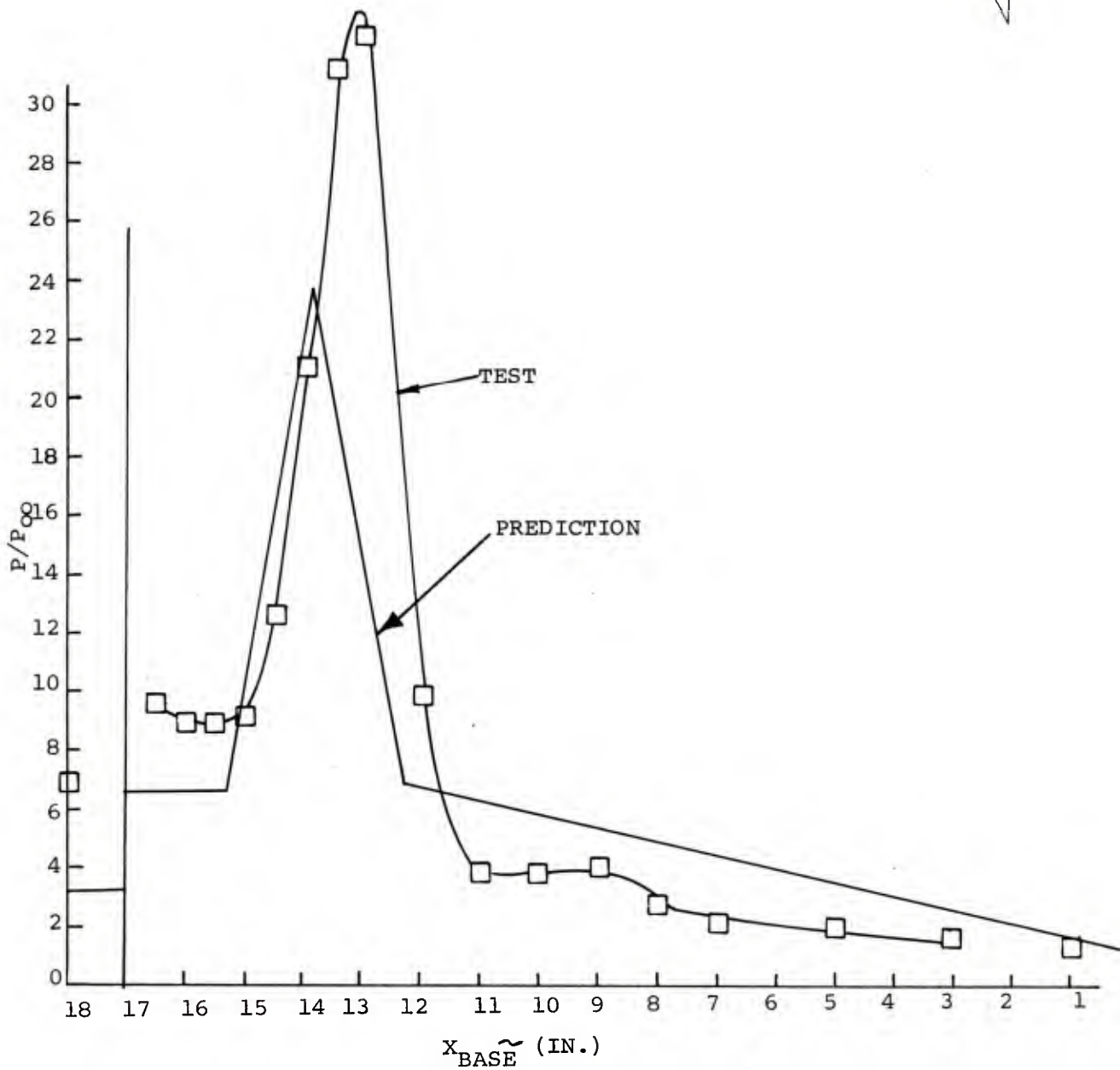
FIGURE 26 – COMPARISON OF PREDICTED AND EXPERIMENTAL
PROJECTILE PRESSURES FOR PT109, $\Delta y = 1"$, $\alpha = 0°$

PROJECTILE SURFACE PRESSURE DATA

PREDICTION

TEST

X_{BASE} (IN.)
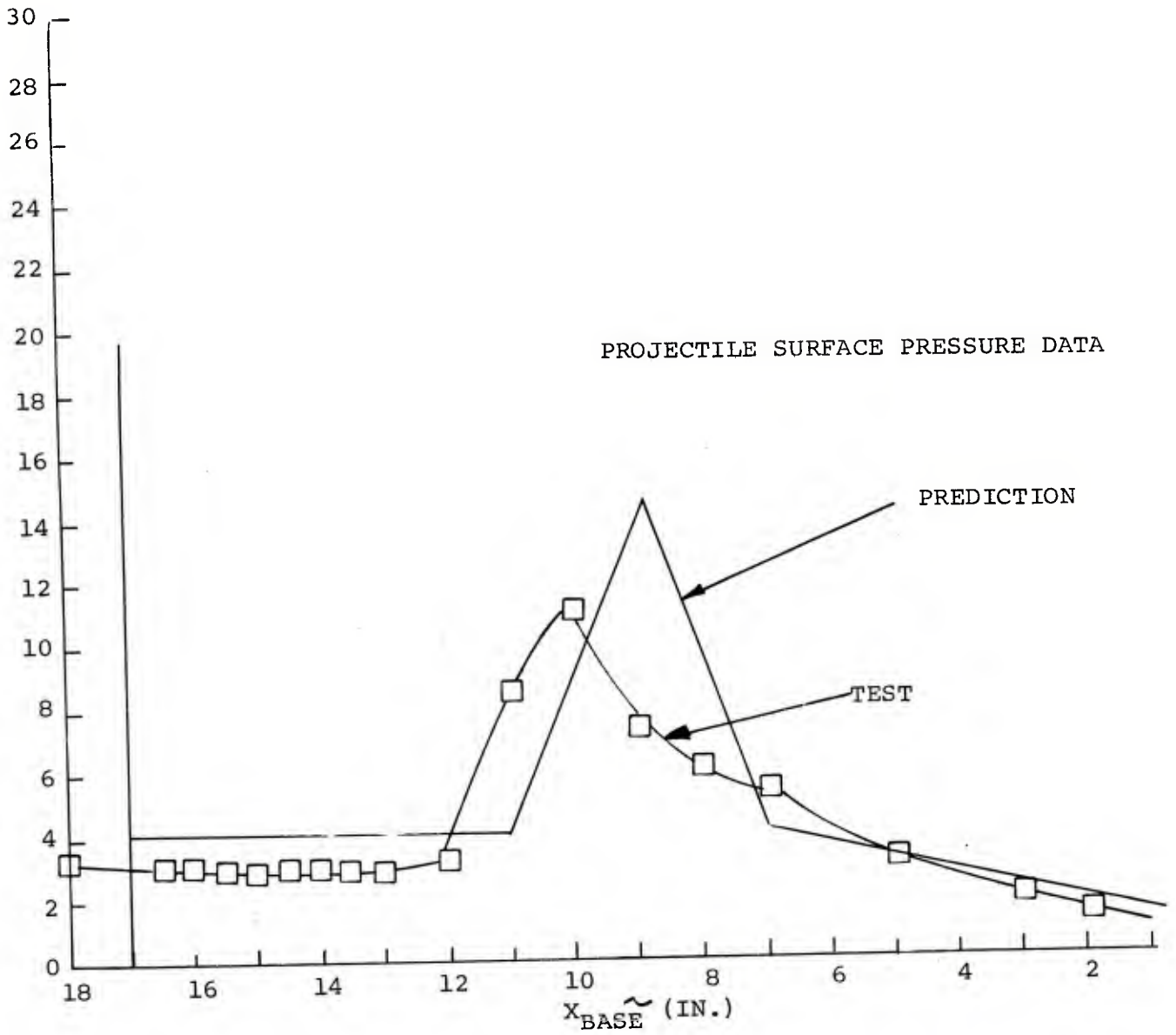
FIGURE 27 - COMPARISON OF PREDICTED AND EXPERIMENTAL
PROJECTILE PRESSURE FOR PT116, $\triangle Y = 4.5"$, $\alpha = 0°$

FIGURE 28 - COMPARISON OF PREDICTED AND EXPERIMENTAL PROJECTILE PRESSURES FOR PT150, $\triangle y = 0.5"$, $\alpha = 8°$
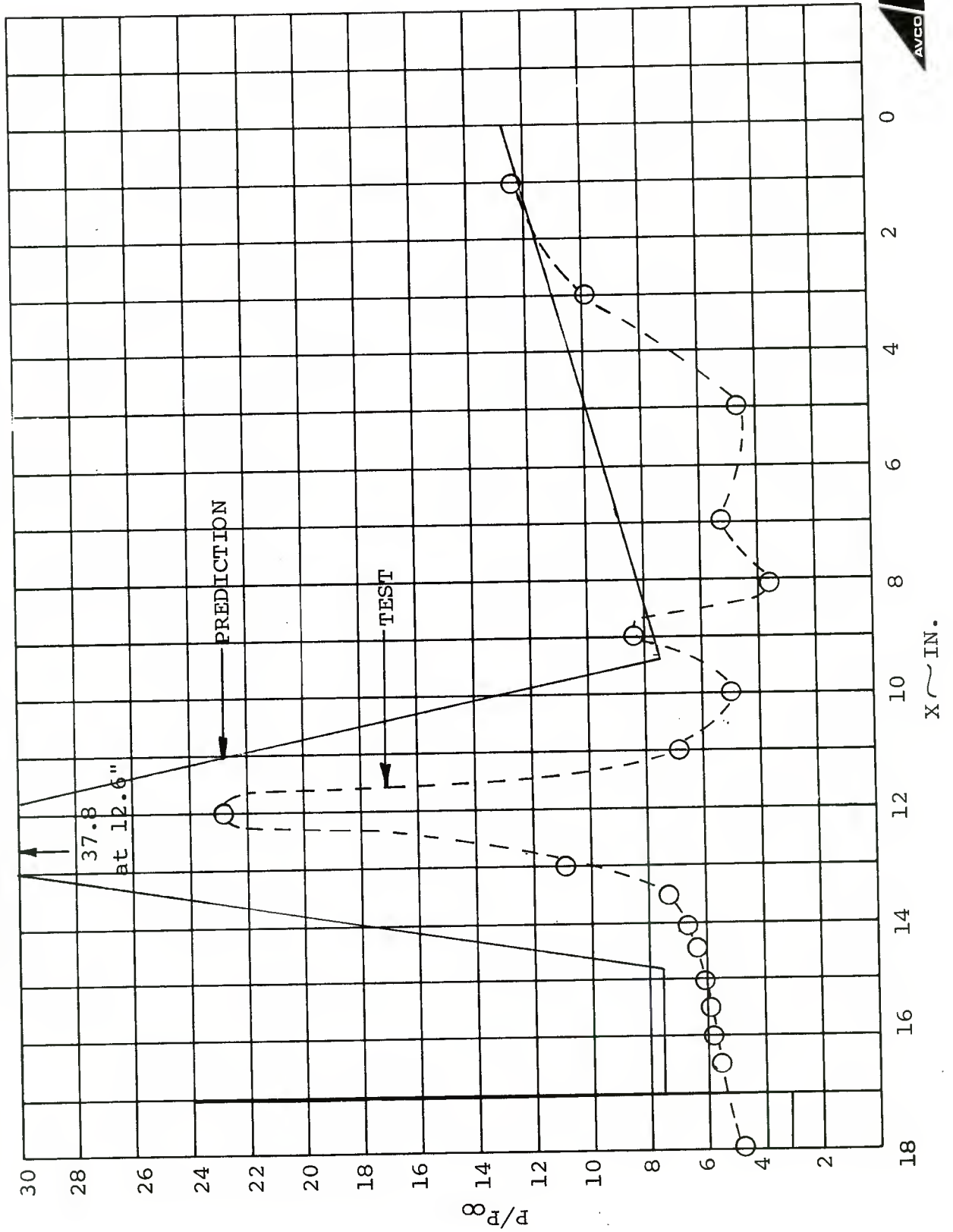
FIGURE 29 – COMPARISON OF PREDICTED AND EXPERIMENTAL
PROJECTILE PRESSURES FOR PT149, $\Delta y = 1"$, $\alpha = 8°$
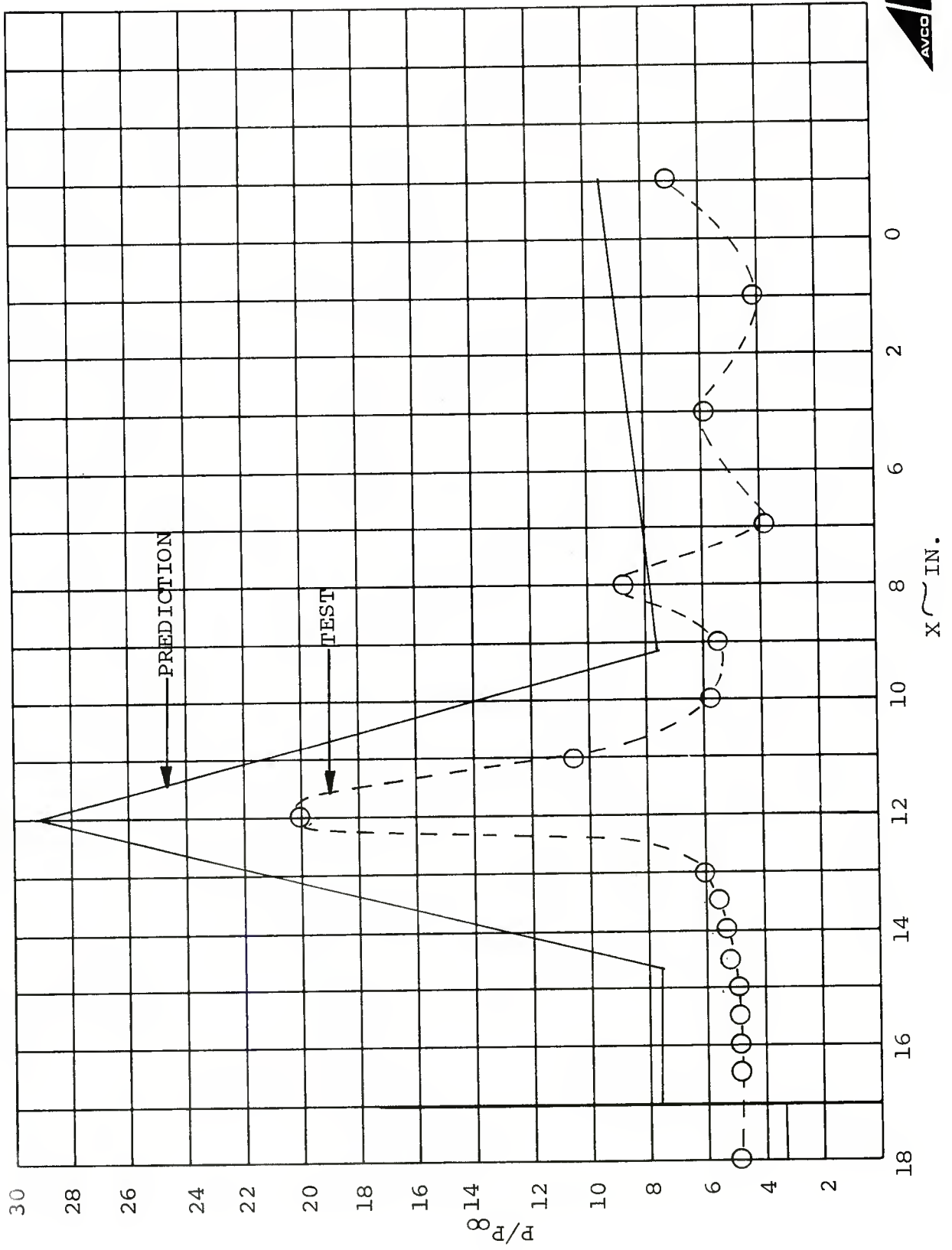
FIGURE 30 - COMPARISON OF PREDICTED AND EXPERIMENTAL PROJECTILE PRESSURES FOR PT147, $\Delta y = 2"$, $\alpha = 8°$
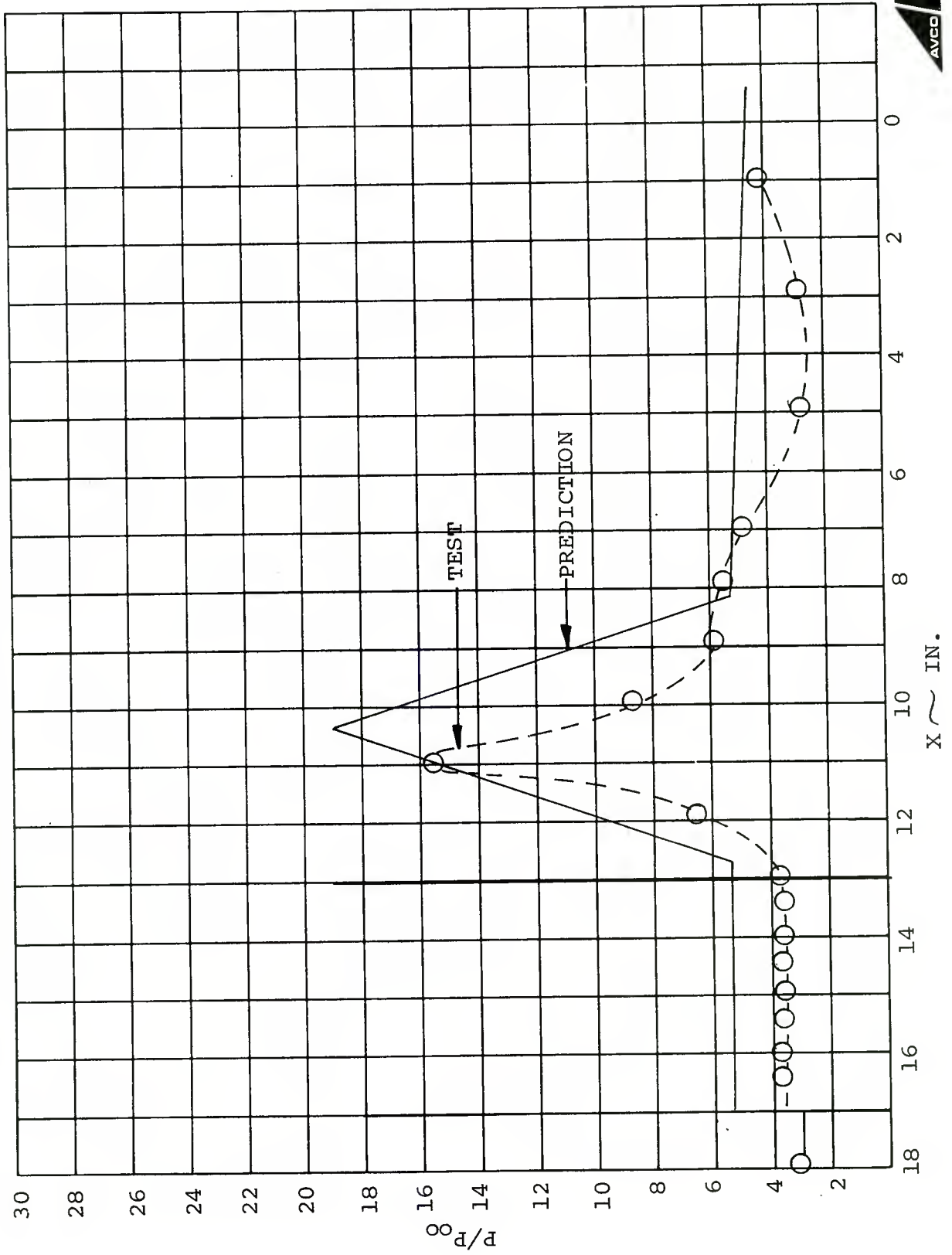
FIGURE 31 - COMPARISON OF PREDICTED AND EXPERIMENTAL PROJECTILE PRESSURES FOR PT145, $\Delta y = 4"$, $\alpha = 8°$
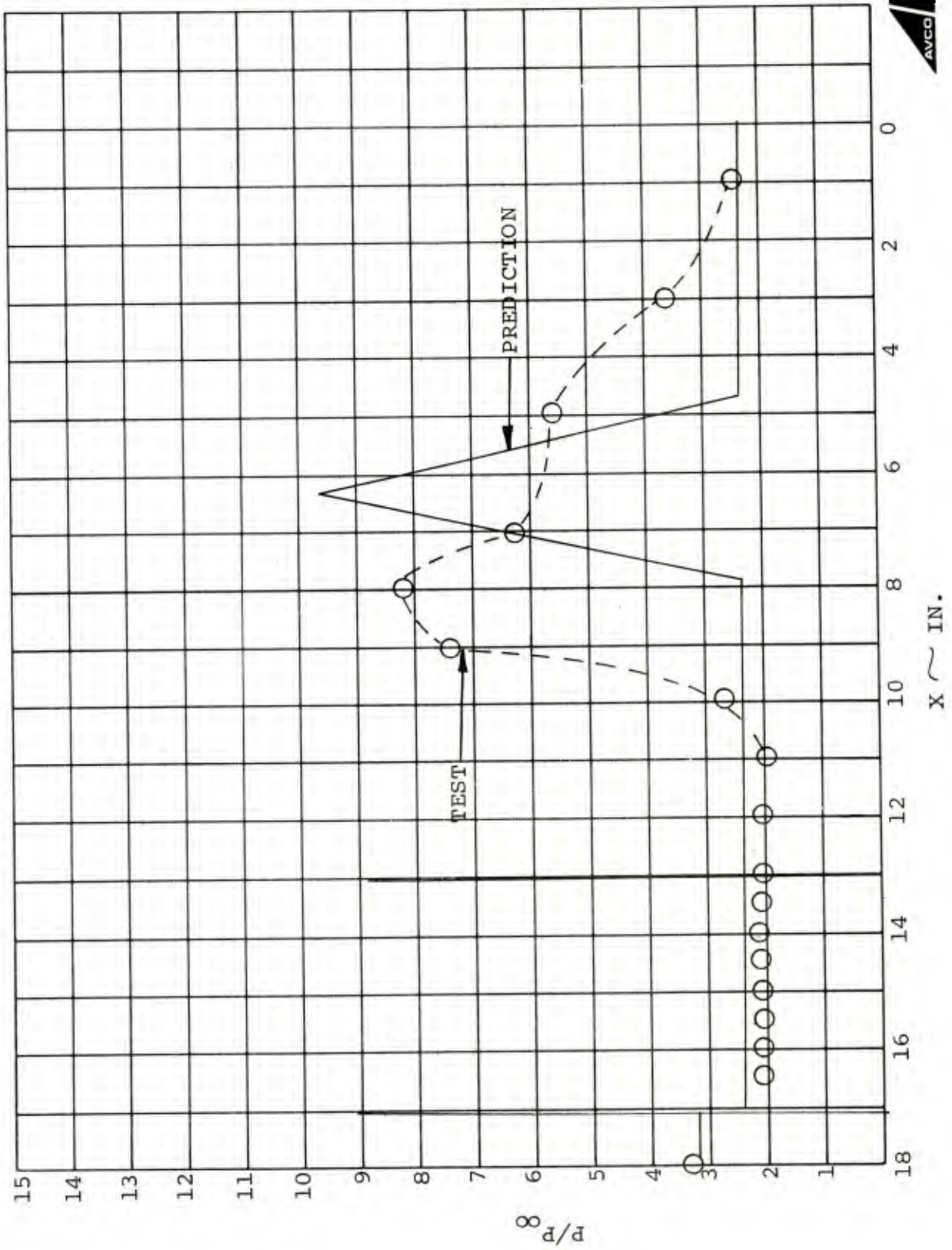
clearly indicate the presence of high peak pressures. The model will predict these pressure overshoots (above normal shock values) at separations and incidences which are somewhat different than observed in the test data. Thus, the model results can be thought of as slightly "time-shifted" when applied to the transient discard process.

Figures 32 - 35 present the large angle of attack data. The tendency to overpredict peak pressure and underpredict location is again evident. Note that the sabot bow shock is not predicted to hit the projectile surface for the larger separation cases. This is in agreement with the test data for the largest separation distance, but disagrees for the $\triangle y = 4$ inch case. This discrepancy can be ascribed to the neglect of shock interaction effects on the sabot bow shock shape. (That is, the projectile bow shock and shoulder expansion waves will modify the sabot shock from its isolated flight behavior). This mismatch between data and theory again can be translated into a time displacement equivalent for the actual transient discard process. Lastly, it should be noted that the outlet station behavior for these high incidence cases, as well as the intermediate angle data presented previously, reflect the trend noted before for the large separation distance behavior to asymptote toward the zero incidence values for a fixed incidence.

FIGURE 32 - COMPARISON OF PREDICTED AND EXPERIMENTAL
PROJECTILE PRESSURES FOR PT190, $\triangle Y = 1"$, $\alpha = 18°$
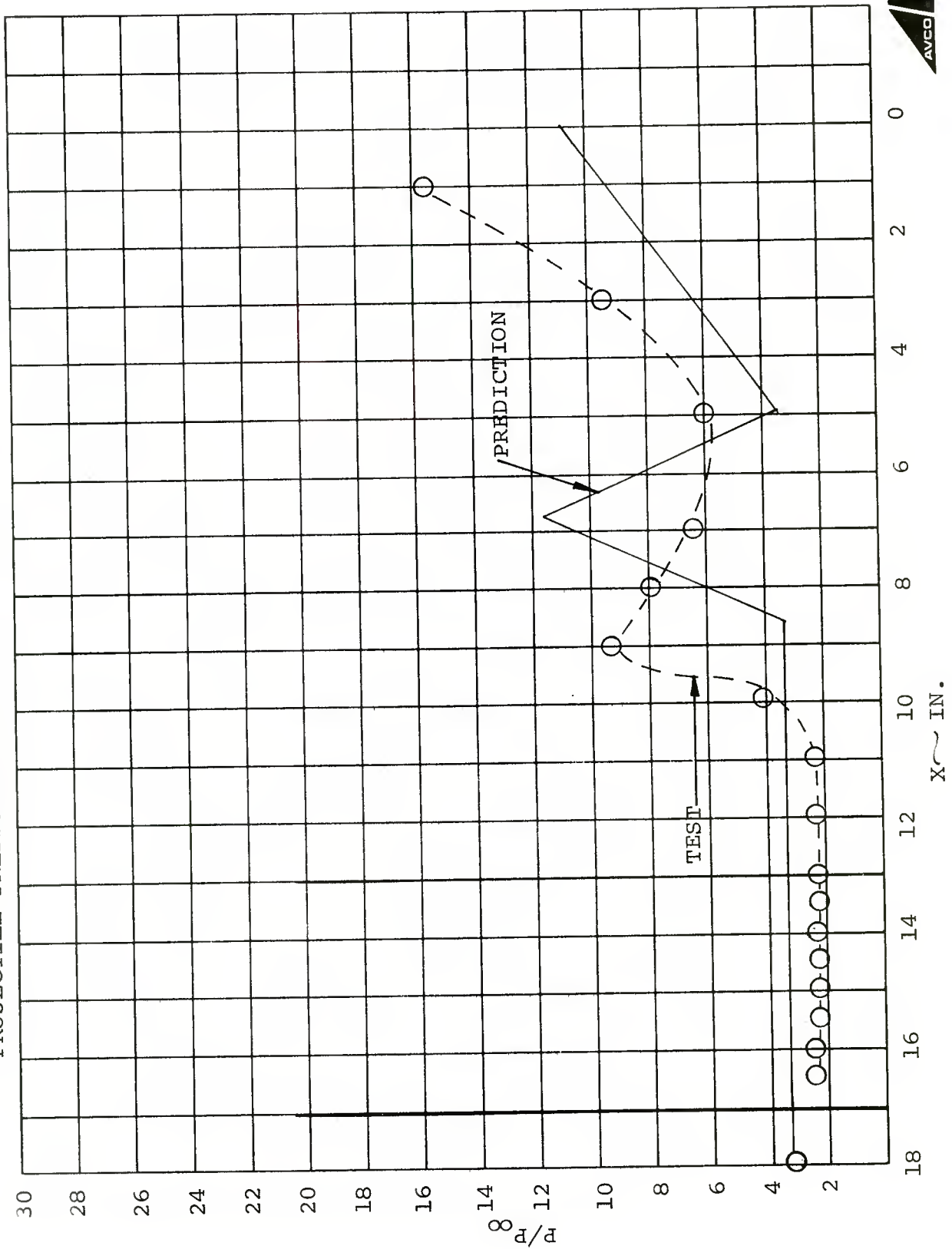
FIGURE 33 - COMPARISON OF PREDICTED AND EXPERIMENTAL PROJECTILE PRESSURES FOR PT188, $\Delta Y = 2''$, $\alpha = 18^{o}$
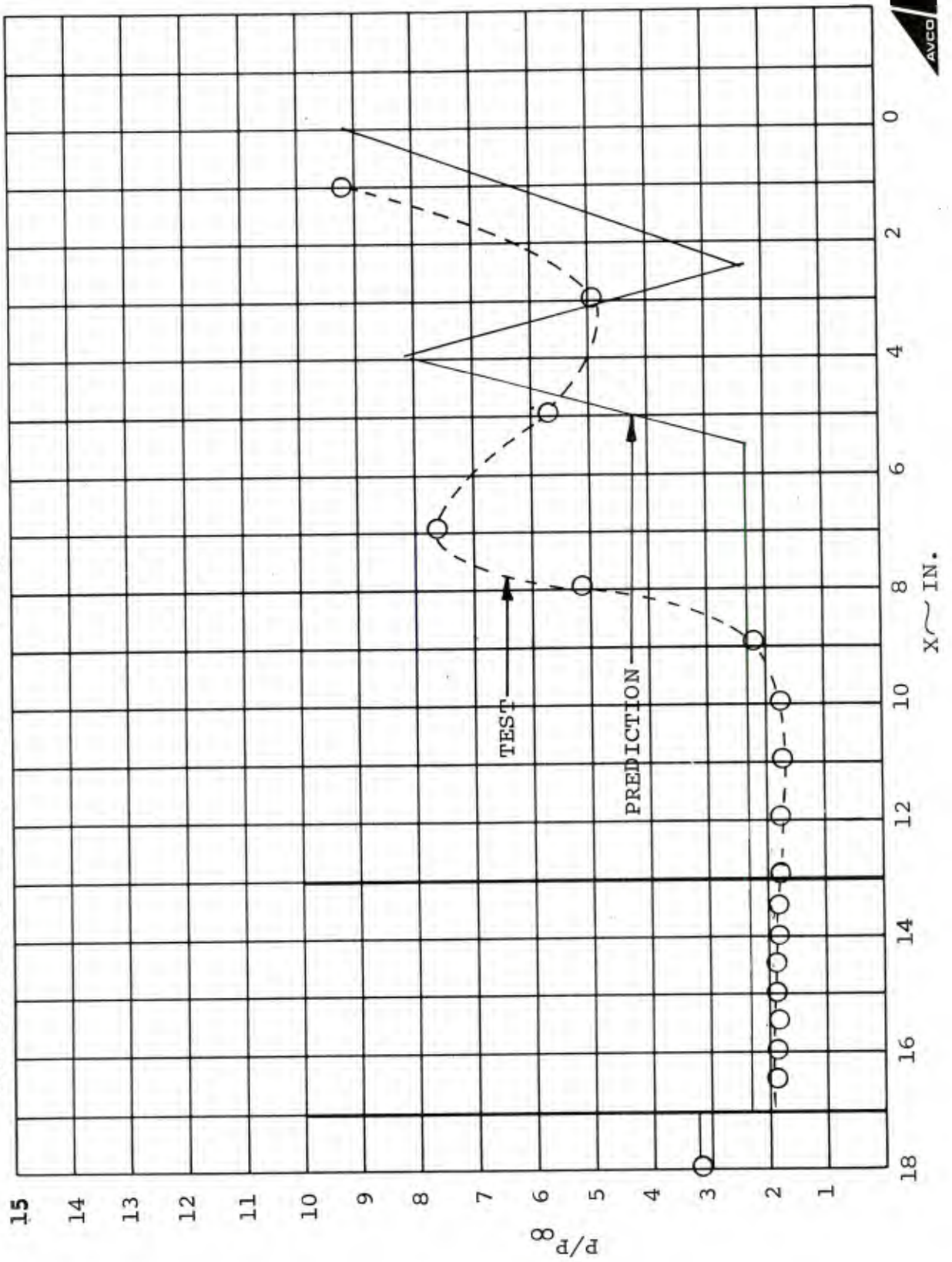
FIGURE 34 - COMPARISON OF PREDICTED AND EXPERIMENTAL PROJECTILE PRESSURES FOR PT186, $\Delta y = 4"$, $\alpha = 18°$
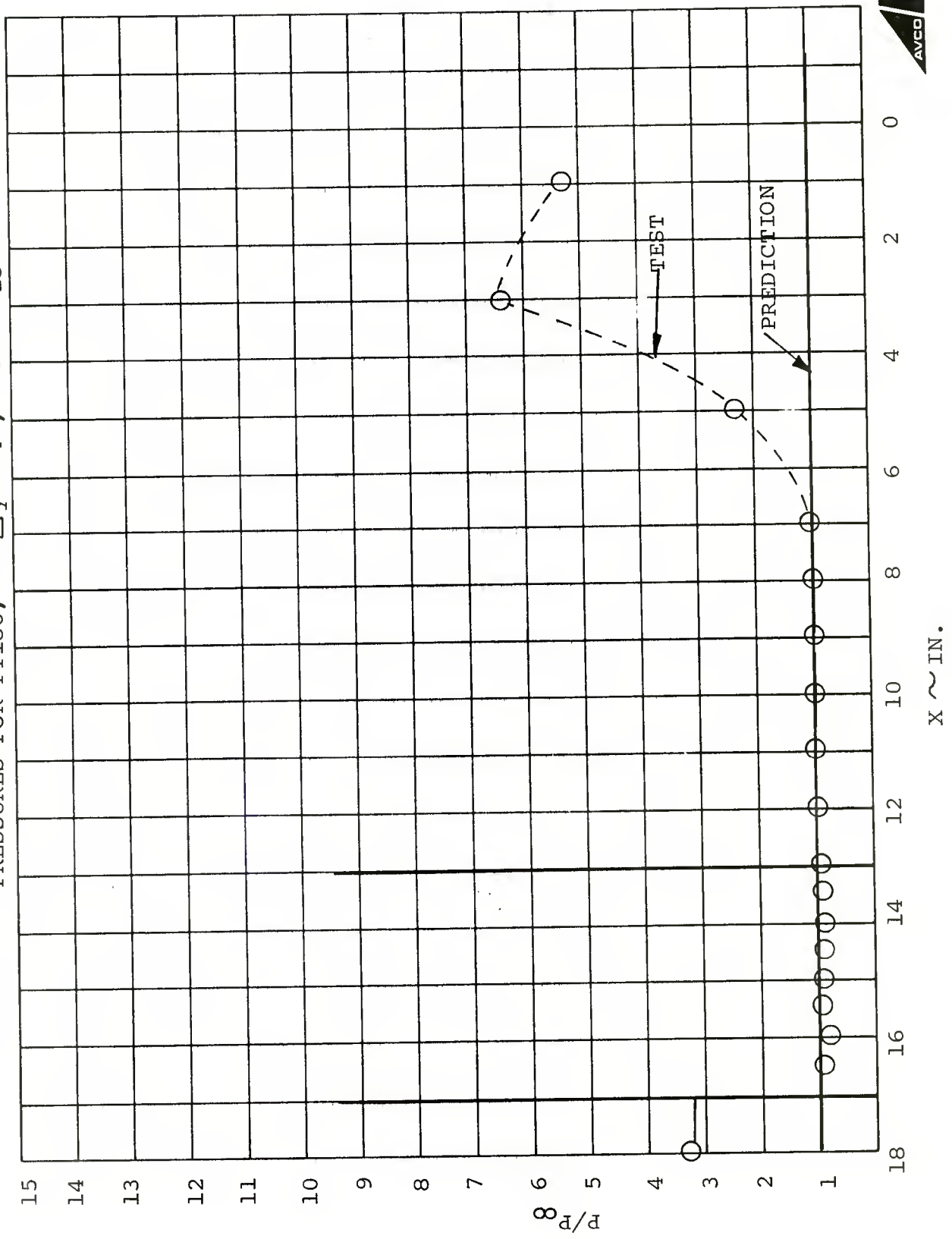
FIGURE 35 - COMPARISON OF PREDICTED AND EXPERIMENTAL PROJECTILE PRESSURES FOR PT184, $\Delta Y = 6"$, $\lambda = 180$
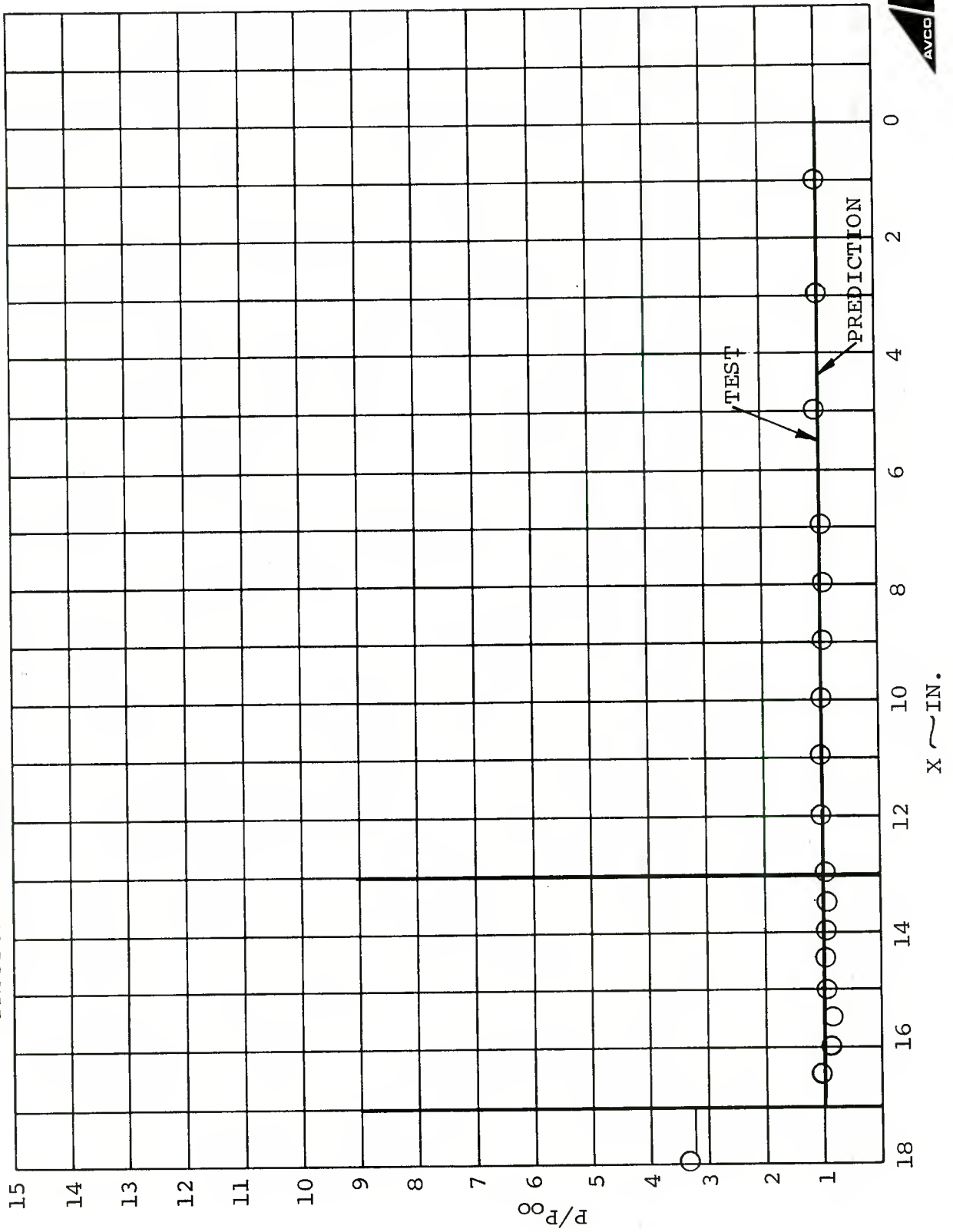
4.2 SABOT DISCARD DYNAMIC MOTION COMPARISONS

The projectile and sabot analyzed are sketched separately in Figure 36. The front face of the actual sabot is not, in fact, conical, but rather has the form indicated by the dashed line in the figure.* The projectile is approximately eleven inches long, its cylindrical body is 0.81 inches in diameter, the mass center is 7.3 inches from the base, the pitch inertia is 0.00619 slug-ft^2, the roll inertia is 4.996 x 10^{-5} slug-ft^2, and C_{M_α} is -18 rad^{-1}, reference area and length being 0.00358 ft^2 and 0.0675 ft., respectively.

Inertial and geometric parameters for a sabot petal are listed in Table 1. The variations of the Newtonian lift, drag and moment coefficients, denoted C_L, C_D and C_M, respectively, with angle of attack are plotted in Figure 37. Reference area and length are the same as for the projectile. The moment coefficient is with respect to the mass center, and is positive for a nose-up moment (i.e., proportional to $-M_x$). The velocity of the round at the muzzle was taken to be 5150 ft/sec.

Composite x-ray photographs of the separation process provided by the U. S. Army Ballistic Research Laboratories are shown in Figure 38. Figure 39 presents the results obtained

---

*Assuming constant pressure, the pitching moment contribution of the assumed conical front face is twelve percent lower than that of the actual front face.
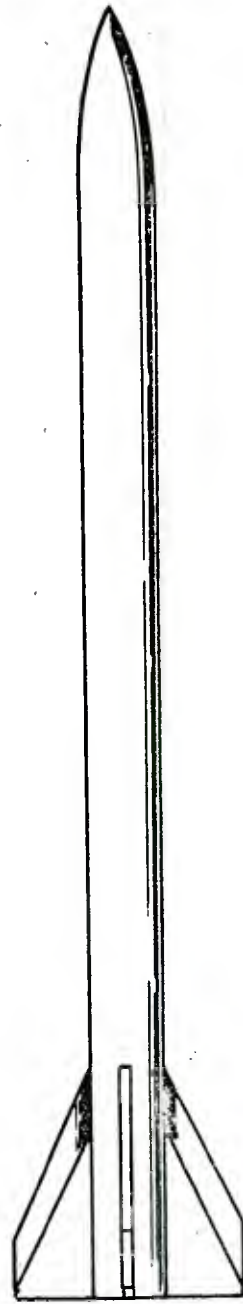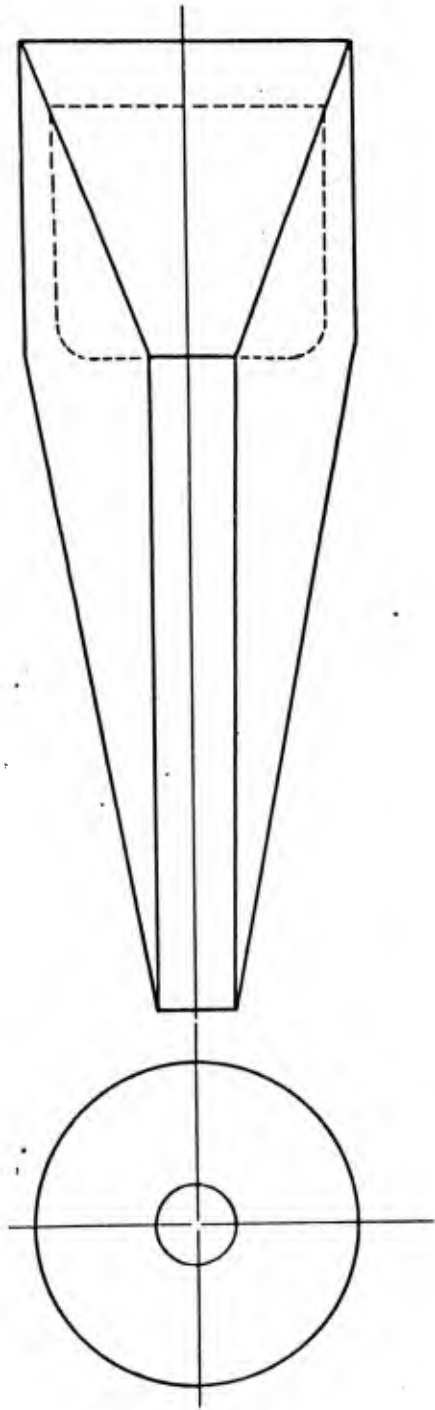
FIGURE 36 - SABOT AND PROJECTILE CONFIGURATIONS ANALYZED

TABLE I

SABOT SEGMENT INERTIAL AND GEOMETRIC PARAMETERS

PARAMETER	VALUE
m	.013556 slugs
I_x	$.30764 \times 10^{-3}$ slug-ft^2
I_y	$.31818 \times 10^{-3}$ slug-ft^2
I_z	$.25541 \times 10^{-4}$ slug-ft^2
I_{yz}	$.31303 \times 10^{-4}$ slug-ft^2
η	.073756 ft.
ζ	.45242 ft.
r_i	.03375 ft.
r_o	.12292 ft.
l_i	.50161 ft.
ϕ_o	45 deg.
θ_f	160 deg.
θ_b	169.92 deg.
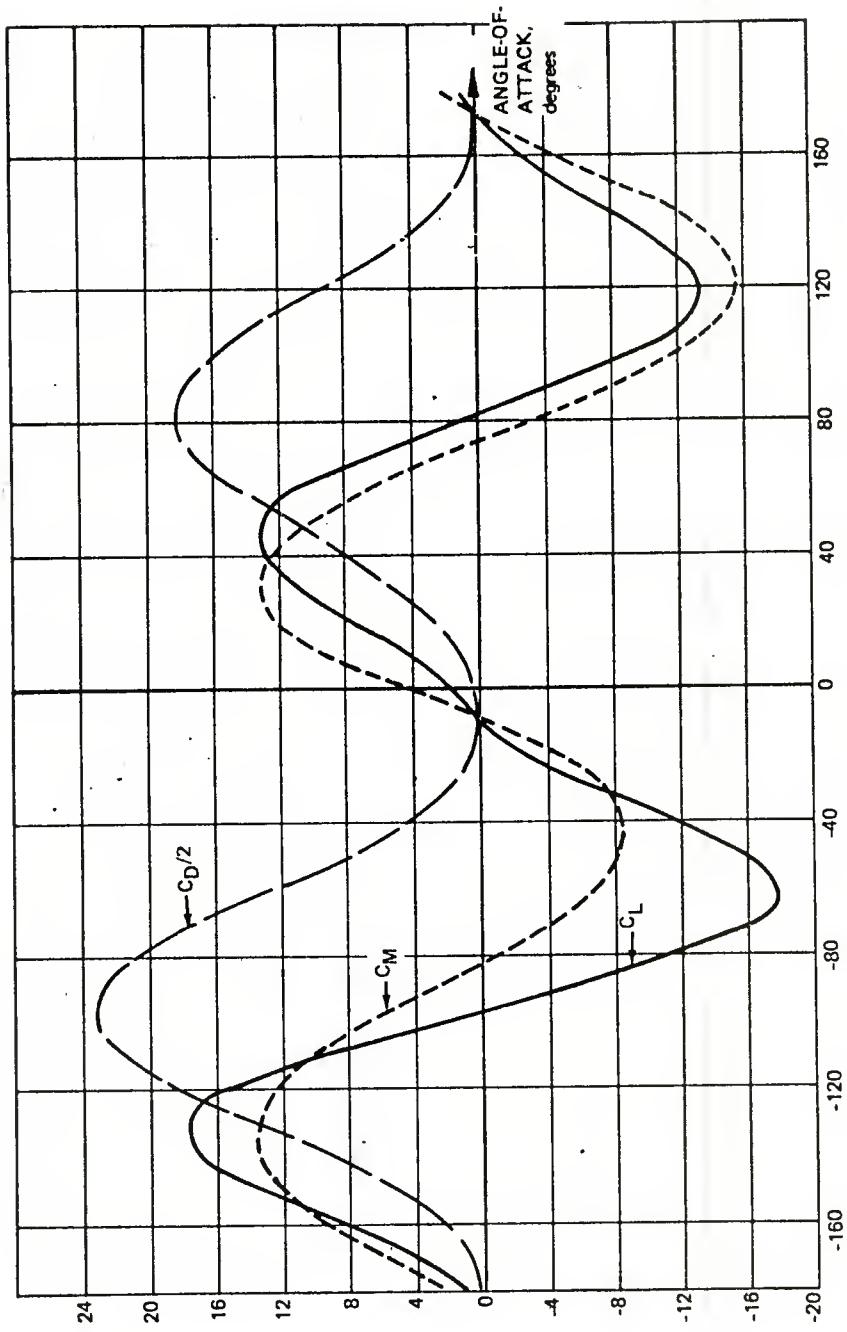
FIGURE 37 - LIFT, DRAG AND MOMENT COEFFICIENTS OF SABOT SEGMENT ANALYZED

$V_pT = 1$ ft
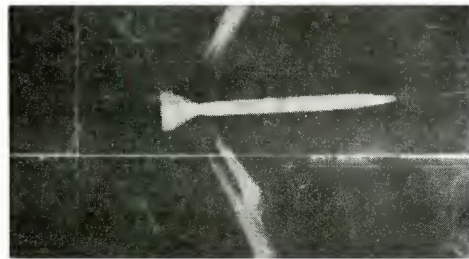
$V_pT = 16.8$ ft

$V_pT = 4.2$ ft
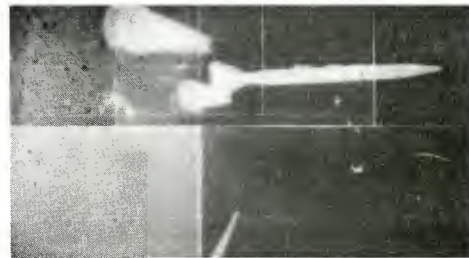
$V_pT = 21.2$ ft

$V_pT = 9.6$ ft

$V_pT = 26.2$ ft

FIGURE 38 - Composite X-Ray Photographs of Sabot Discard
Provided by Ballistic Research Laboratory,
ARRADCOM, Aberdeen Proving Ground, MD
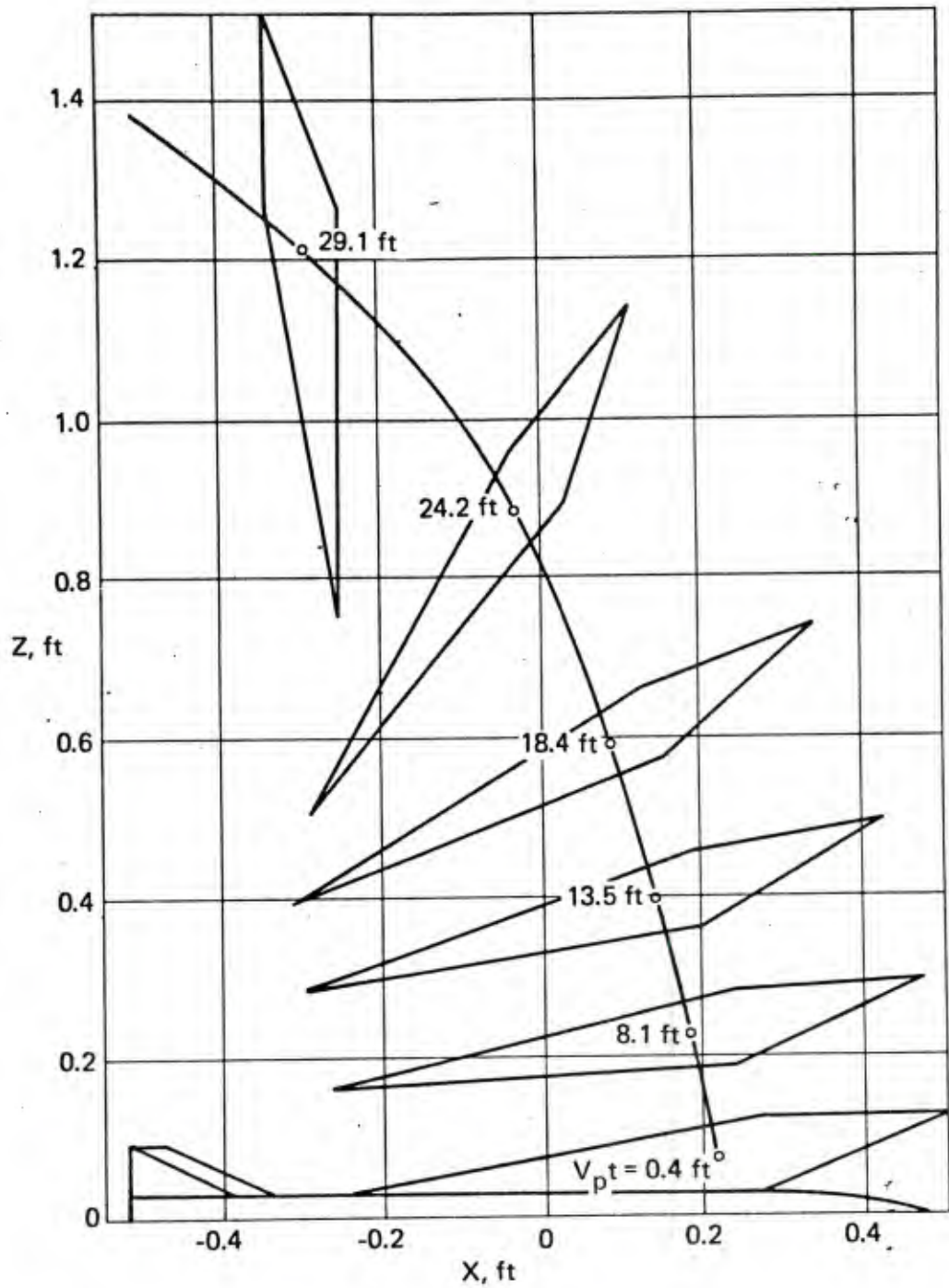
FIGURE 39 – SABOT SEGMENT TRAJECTORY FOR SYMMETRIC DISCARD,
ZERO INITIAL SPIN RATE (ORIGINAL MODEL)

previously (with the original interaction flow field model).
It is clear that these original predictions significantly
underpredict the rotation of the sabot petals at a given
distance from the muzzle. Alternately, the lateral separation
between the sabot and the projectile is significantly over-
estimated for a fixed degree of rotation. This behavior arose
because the simple initial interaction model imposed a uniform
pressure over the sabot during most of the interacting flow
phase of the discard process.

Figure 40 presents the sabot segment trajectory com-
puted using the present, improved interaction model, in-
corporating the modeling extensions discussed in the Appendix.
It is clear that the non-uniform pressure distribution presently
available has greatly improved the prediction of the pitching
motion. It appears, in fact, that the pitching motion is now
somewhat overpredicted. This discrepancy may be due to the
presence of some spin or tip-off effects for the actual firing.
It is also noted that mechanical interaction is now predicted
to be present during a significant portion of the discard.
The sabot trailing edge does not lift off of the projectile
surface until 9 feet of travel. This is in marked contrast
to the earlier results,[1] wherein the sabot was predicted to lift
free of the projectile after only 0.5 ft. of travel.

FIGURE 40 - SABOT SEGMENT TRAJECTORY FOR SYMMETRIC DISCARD, ZERO INITIAL SPIN RATE (IMPROVED MODEL)
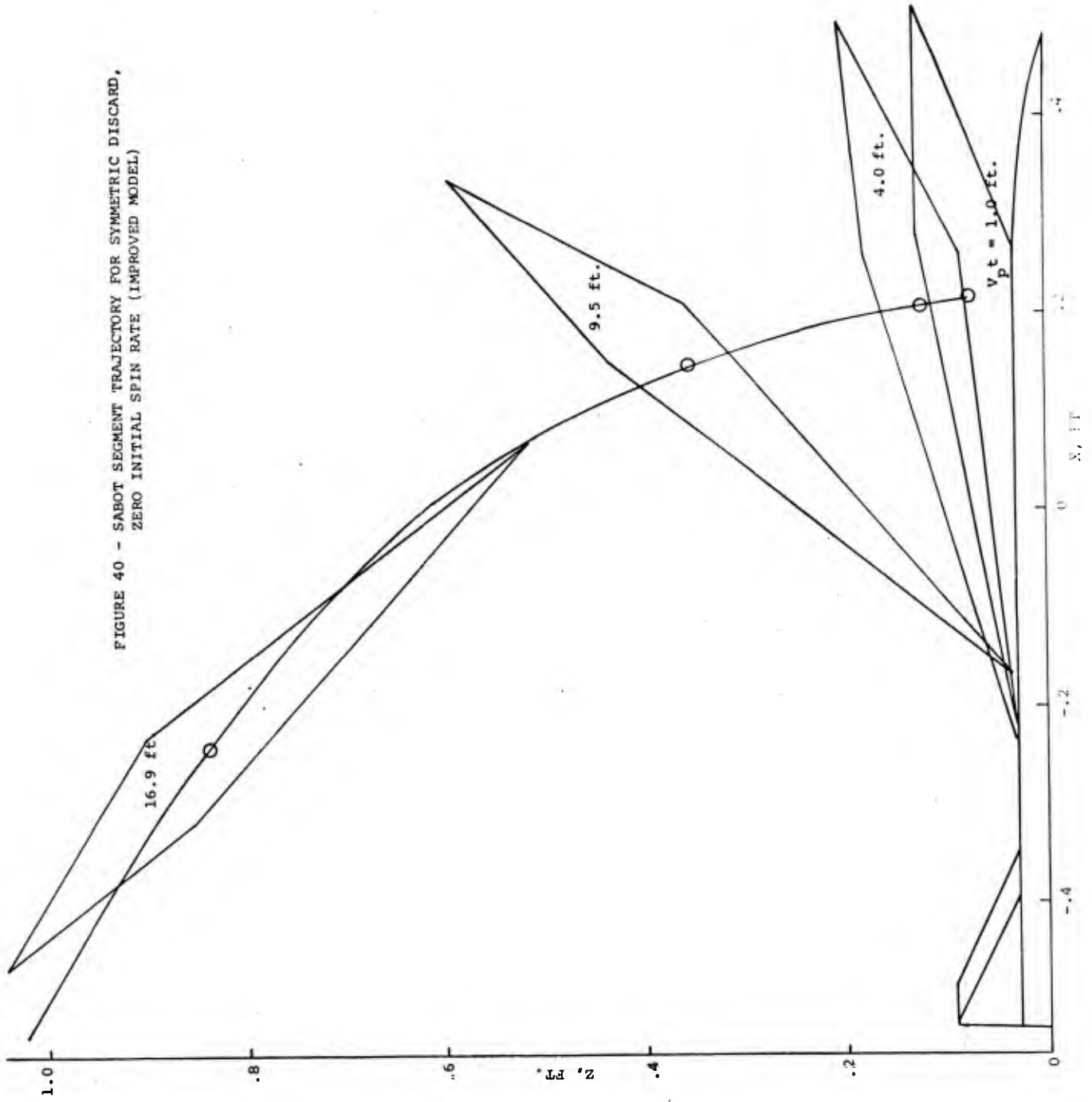
5.0 CONCLUSIONS AND RECOMMENDATIONS

Experimental wind tunnel test data generated by BRL has been used to formulate and verify an improved engineering model of the interaction flow field which develops about the projectile/sabot petal package during the sabot discard process. It has also been found that this improved flow field representation results in improved prediction of the transient discard process observed by BRL using x-ray photography techniques for one particular high energy round.

It is felt that this up-graded analysis can provide a sound point of departure for further development of an accurate tool for assessing the influence of sabot, projectile and launch parameters upon aerodynamically induced near field projectile dispersions. The following specific recommendations appear germane:

(1) The most important aspect of the interaction process which remains to be described is the interaction between the discarding sabot petals and the stabilizing fins present for fin-stabilized rounds. It is suggested that generation of experimental data addressing this question be a high priority future task. In the event that such data cannot be generated in a timely manner, a viable alternative is to proceed with simplified preliminary modeling task which could be refined at a later date.

(2)   The data obtained to date have permitted a high
degree of improvement in our understanding of the inter-
action flow field.   However, the test data were generated
for only one configuration and therefore extrapolation to other
configurations does still involve some degree of risk.   It
is therefore suggested that additional testing be performed
wherein significant design parameters are varied in order
to permit construction and verification of a completely
general model.

REFERENCES

1. Crimi, P., and Siegelman, D., "Analysis of Mechanical and Gasdynamic Loadings during Sabot Discard from Gun-Launched Projectiles," BRL Contract Report No. 341, June 1977.

2. Schmidt, E., "Wind Tunnel Measurements of Sabot Discard Aerodynamics," BRL Report in preparation.

3. Holden, M. S., "Experimental Studies of Separated Flows at Hypersonic Speeds. Part I: Separated Flows over Axisymmetric Spiked Bodies," AIAA J., Vol. 4, No. 4, pp. 591-599, April 1966.

4. Edney, B. E., "Effects of Shock Impingement on the Heat Transfer Around Blunt Bodies," AIAA J., Vol. 6, No. 1, pp. 15 - 21, Jan. 1968.

5. Hains, F., and Keyes, J., "Shock Interferrence Heating in Hypersonic Flows," AIAA J., Vol. 10, No. 11, pp. 1441-1447, Nov. 1972.

6. Reeves, B. L., et. al., "Hypersonic Flow Over Indented Nosetips," AIAA Paper No. 77-91, AIAA 15th Aerospace Sciences Meeting, Los Angeles, Calif., Jan. 24 - 26, 1977.

7.   "Equation, Tables, and Charts for Compressible Flow,"
      NACA Report 1135, 1953.

8.   Hayes, W. D., and Probstein, R. F., Hypersonic Flow
      Theory, Chapter III, pp. 70-92, Academic Press, N. Y.,
      1959.

9.   Thomke, G. J., and Roshko, A., "Incipient Separation of
      a Turbulent Boundary Layer at High Reynolds Number
      in Two-Dimensional Supersonic Flow over a Compression
      Corner," NASA DAC-59819, Jan. 1969.

10.   Hunter, L. G., and Reeves, B. L., "Results of a Strong
      Interaction, Wake-Like Model of Supersonic Separated
      and Reattaching Turbulent Flows," AIAA J., Vol. 9,
      No. 4, pp. 703-712, April 1971.

11.   Law, H. C., "Supersonic Shock Wave Turbulent Boundary
      Layer Interaction," AIAA J., Vol. 14, No. 6,
      pp. 730-734, June 1976.

12.   Moretti, G., and Abbett, M., "A Time-Dependent Computational
      Method for Blunt Body Flows," AIAA J., Vol. 4, No. 12,
      pp. 2136-2141, Dec. 1966.

13.   Moretti, G., and Pandolfi, M., "Analysis of the Inviscid
      Flow about a Yawed Cone," PIBAL Report No. 72-18, May 1972.

APPENDIX

The configuration of interest for the sabot discard computations presented in Section 4.2 utilizes a sabot with a leading edge which lies upstream of the projectile tip, as shown in Figure A.1. This configuration is sufficiently different from the experimental test configuration to require an extension of the interaction flow field modeling, as follows.

Case 1 - <u>Sabot Bow Shock Lies Upstream of Projectile Tip</u>

If the gap between the projectile surface and the sabot underside cannot pass the capture mass flow (see Section 3.1, part (3)) or if the sabot has pitched-up sufficiently to produce a detached bow wave prior to significant deceleration, then a normal shock wave will be present upstream of the projectile tip. In this instance, the projectile surface pressure is modeled by:

(i)   Utilizing the blunt body analogy (see Section 3.1, part (1)) to specify that $P = P_{t_2}$ and $dP/ds = 0$ at the projectile stagnation point, while setting $P = P_2^*$ at the projectile shoulder.

(ii)   Performing a Prandtl-Meyer expansion[7] around the projectile's shoulder to determine the background
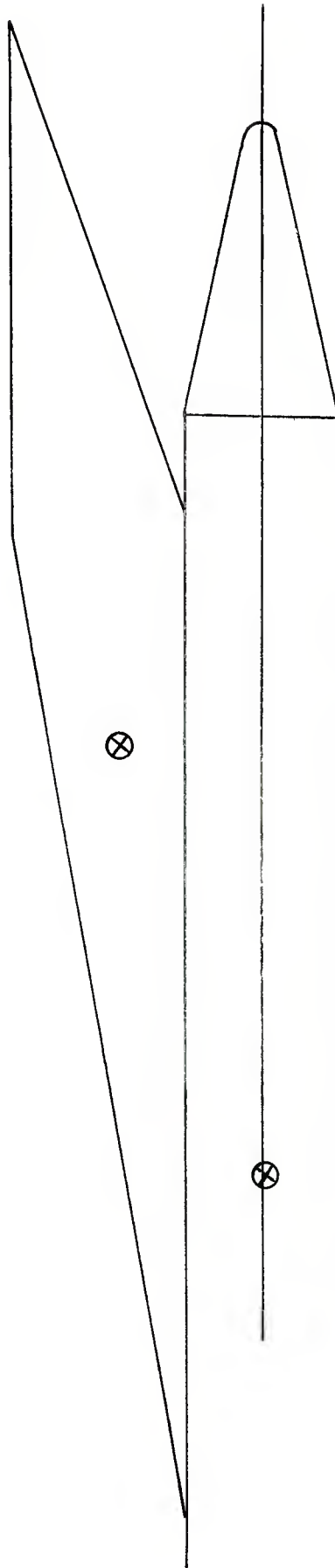
FIGURE A.1 - SABOT DISCARD DYNAMIC MOTION TEST CASE CONFIGURATION

pressure on the projectile surface

$$(P_{cyl} \neq P_{\infty}, M_{cyl} \neq M_{\infty})$$

(iii) Using this background level to assess any

throttling effects in the outlet region

via similar semi-empirical scaling equations as

presented in the text (Section 3.2, parts (6)-(7)

and Section 3.3, Part (6)):

$$\frac{P_{end} - P_{cyl}}{P_{NS2} - P_{cyl}} = .4 \ \alpha/\alpha_{crit} \qquad \text{for } P_{end} \leq P_{NS2}$$

This constant end point pressure is applied over

a zone of length X upstream from the sabot

trailing edge, where

$$X = 0.4 \ (\alpha/\alpha_{crit}) \ (X|_{\alpha/\alpha_{crit}} = 2.5)$$

and where the reference length is determined by

the procedures of Section 3.2, part (5). A

linear pressure increase from P_{cyl} to P_{end} is

assumed over an additional length interval

equal to X.

(iv) Deleting the sabot underside pressure bump (see

Section 3.2, part (2)), since there is no

reflected shock wave present for this case.

Case 2 - <u>Sabot Bow Shock Impinges on Conical Section of Projectile</u>

As the sabot decelerates, the sabot bow shock will translate aft with respect to the projectile. Thus, there will be a time when the sabot bow shock will impinge upon the conical portion of the projectile. The following procedures are then employed.

(i)   Use Newtonian[8] pressures on the projectile nose cap.

(ii)   Use turbulent separation data[9] to evaluate the pressure on the conical section upstream of the shock impingement point (see Section 3.2, part (2) and Section 3.3, part (5)). This pressure level is merged smoothly into the Newtonian cap region. Separation is assumed present only when the pressure downstream of the impinging shock exceeds the separation value (see Section 3.3, part (7).

(iii)   The sabot bow shock wave impingement and reflection is treated by the methods described in Section 3.3, parts (3)-(4). This shock reflection pressure is applied between the projectile shoulder and the shock impingement point.

(iv)   The cylinder surface pressures are found by
        applying procedures (ii)-(iii) described previously
        in the case 1 discussion.

(v)   The sabot underside pressure distribution model
        is unaltered. Specifically, this neglects
        consideration of the possible situation where
        the sabot bow shock reflection off of the pro-
        jectile impinges back on the sabot petal up-
        stream of the sabot corner. This will result
        in an underprediction of the sabot petal pitching
        moment during the phase of removal where such
        a situation could exist.

DISTRIBUTION LIST

No. of Copies	Organization	No. of Copies	Organization
12	Commander Defense Technical Info Ctr ATTN: DDC-DDA Cameron Station Alexandria, VA 22314	6	Commander US Army Armament Research and Development Command ATTN: DRDAR-TSS (2 cys) DRDAR-TDS, Mr. Lindner DRDAR-TDA, Mr. Blick DRDAR-LC-F, Mr. A. Loeb Mr. E. Friedman Dover, NJ 07801
1	Director Defense Nuclear Agency Washington, DC 20305		
2	HQDA (DAMA-WSA, MAJ Csoka: DAMA-CSM, LTC Germann) Pentagon Washington, DC 20310	6	Commander US Army Armament Research and Development Command ATTN: DRDAR-LCV, (Mr. Reisman) DRDAR-SCN, (Mr. Kahn) DRDAR-SCW, (Mr. Townsend) DRDAR-LC, (Dr. Frasier) DRDAR-SG, (Dr. T. Hung) PM, XM788/789, LTC Delany Dover, NJ 07801
1	Director US Army BMD Advanced Technology Center P.O. Box 1500, West Station Huntsville, AL 35807		
1	Commander US Army Ballistic Missile Defense Systems Command Huntsville, AL 35804	1	Commander US Army Armament Materiel Readiness Command ATTN: DRSAR-LEP-L, Tech Lib Rock Island, IL 61299
1	ODCSI, USAREUR & 7A ATTN: AEAGB-PDN (S&E) APO NY 09403	6	Commander US Army Watervliet Arsenal ATTN: DRDAR-LCB-TL Mr. W. Dock Dr. G. Carofano Mr. P. Alto DRDAR-LCB, Mr. T. Allen Mr. R. Billington Watervliet, NY 12189
1	Commander US Army Materiel Development and Readiness Command ATTN: DRCDMD-ST 5001 Eisenhower Avenue Alexandria, VA 22333		
1	Commander US Army Materiel Development and Readiness Command ATTN: DRCDL 5001 Eisenhower Avenue Alexandria, VA 22333	3	Commander US Army Aviation Research and Development Command ATTN: DRSAV-E DRCPM-AAH Product Manager, AH-1 P.O. Box 209 St. Louis, MO 63166

81

DISTRIBUTION LIST

No. of Copies	Organization	No. of Copies	Organization
1	Director US Army Air Mobility Research and Development Laboratory Ames Research Center Moffett Field, CA 94035	1	Commander US Army Materiels and Mechanics Research Center ATTN: DRXMR-ATL Watertown, MA 02172
1	Commander US Army Communications Rsch and Development Command ATTN: DRDCO-PPA-SA Fort Monmouth, NJ 07703	1	Commander US Army Research Office ATTN: CRD-AA-EH P.O. Box 12211 Research Triangle Park NC 27709
1	Commander US Army Electronics Research and Development Command Technical Support Activity ATTN: DELSD-L Fort Monmouth, NJ 07703	2	Director US Army TRADOC Systems Analysis Activity ATTN: ATAA-SL, Tech Lib ATAA-S White Sands Missile Range, NM 88002
4	Commander US Army Missile Command ATTN: DRDMI-R DRDMI-RBL DRDMI-RDK DRDMI-YDL Redstone Arsenal, AL 35809	3	Commander Naval Air Systems Command ATTN: AIR-604 Washington, DC 20360
1	Commander US Army Natick Research and Development Command ATTN: DRXRE, Dr. D. Sieling Natick, MA 01762	3	Commander Naval Ordnance Systems Cmd ATTN: ORD-9132 Washington, DC 20360
1	Commander US Army Tank Automotive Research & Development Cmd ATTN: DRDTA-UL Warren, MI 48090	2	Commander David W. Taylor Naval Ship Research & Development Center ATTN: Lib Div, Code 522 Aerodynamic Lab Bethesda, MD 20084
1	Commander US Army Jefferson Proving Ground ATTN: STEJP-TD-D Madison, IN 47250	3	Commander Naval Surface Weapons Center ATTN: Code 6X Mr. F.H. Maille Dr. J. Yagla Dr. G. Moore Dahlgren, VA 22448

DISTRIBUTION LIST

No. of Copies	Organization
1	Commander Naval Surface Weapons Center ATTN: Code 730, Tech Lib Silver Spring, MD 20910
1	Commander Naval Weapons Center ATTN: Code 553, Tech Lib China Lake, CA 93555
1	Commander Naval Research Laboratory ATTN: Tech Info Div Washington, DC 20375
1	Commander Naval Ordnance Station ATTN: Code FS13A, P. Sewell Indian Head, MD 20640
1	AFRPL/LKCB, Dr. Horning Edwards AFB, CA 93523
2	AFATL (DLDL, Dr. D.C. Daniel; Tech Lib) Eglin AFB, FL 32542
1	AFWL/DEV Kirtland AFB, NM 87117
1	ASD/XRA (Stinfo) Wright-Patterson AFB, OH 45433
1	Director National Aeronautics and Space Administration George C. Marshall Space Flight Center ATTN: MS-I, Lib Huntsville, AL 38512
1	Director Jet Propulsion Laboratory ATTN: Tech Lib 2800 Oak Grove Drive Pasadena, CA 91103

No. of Copies	Organization
1	Director National Aeronautics and Space Administration Langley Research Center ATTN: MS 185, Tech Lib Langley Station Hampton, VA 23365
1	Director NASA Scientific & Technical Information Facility ATTN: SAK/DL P.O. Box 8757 Baltimore/Washington International Airport, MD 21240
1	AAI Corporation ATTN: Dr. T. Stastny Cockeysville, MD 21030
1	Advanced Technology Labs ATTN: Mr. J. Ranlet Merrick & Steward Avenue Westbury, NY 11590
1	Aerospace Corporation ATTN: Dr. T. Taylor P.O. Box 92957 Los Angeles, CA 90009
1	ARO, Inc. ATTN: Tech Lib Arnold AFS, TN 37389
1	ARO, Inc. Von Karman Gasdynamics Facility ATTN: Dr. J. Adams Arnold AFS, TN 37389
1	ARTEC Associates, Inc. ATTN: Dr. S. Gill 26046 Eden Landing Road Hayward, CA 94545

83

DISTRIBUTION LIST

No. of Copies	Organization	No. of Copies	Organization
2	AVCO Associates, Inc. ATTN: Dr. W. Reinecke Dr. D. Siegelman 201 Lowell Street Wilmington, MA 01887	1	Winchester-Western Division Olin Corporation New Haven, CT 06504
1	Battelle Columbus Laboratories ATTN: J.E. Backofen, Jr. 505 King Avenue Columbus, OH 43201	1	Rockwell Int'l Science Center ATTN: Dr. Norman Malmuth P.O. Box 1085 1000 Oaks, CA 91360
1	Technical Director Colt Firearms Corporation 150 Huyshope Avenue Hartford, CT 14061	1	Sandia Laboratories ATTN: Aerodynamics Dept Org 5620, R. Maydew Albuquerque, NM 87115
1	Flow Simulations, Inc. ATTN: Dr. J. Steger 735 Alice Ave Mountain View, CA 94041	1	S&D Dynamics, Inc. ATTN: Dr. M. Soifer 755 New York Avenue Huntington, NY 11743
2	General Electric Corporation Armaments Division ATTN: Mr. R. Whyte Mr. J. MacNeil Lakeside Avenue Burlington, VT 05401	1	Guggenheim Aeronautical Lab California Institute of Tech ATTN: Tech Lib Pasadena, CA 91104
1	Honeywell, Inc. ATTN: Mail Station MN 112190 (G. Stilley) 600 Second Street, North Hopkins, MN 55343	1	Franklin Institute ATTN: Tech Lib Race & 20th Streets Philadelphia, PA 19103
1	Hughes Helicopter Company Bldg. 2, MST22B ATTN: Mr. R. Forker Centinella and Teel Streets Culver City, CA 90230	1	Director Applied Physics Laboratory The Johns Hopkins University Johns Hopkins Road Laurel, MD 20810

1	Martin Marietta Aerospace
	ATTN: Mr. A.J. Culotta
	P.O. Box 5387
	Orlando, FL 32805
		1	Massachusetts Institute of
			    Technology
			Dept of Aeronautics and
			    Astronautics
			ATTN: Tech Lib
			77 Massachusetts Avenue
			Cambridge, MA 02139

No. of Copies	Organization	No. of Copies	Organization
1	Ohio State University Dept of Aeronautics and Astronautical Engineering ATTN: Tech Lib Columbus, OH 43210		
2	Polytechnic Institute of New York Graduate Center ATTN: Tech Lib Dr. G. Moretti Route 110 Farmingdale, NY 11735		
1	Director Forrestal Research Center Princeton University Princeton, NJ 08540		
1	Southwest Research Institute ATTN: Mr. Peter S. Westine P.O. Drawer 28510 8500 Culebra Road San Antonio, TX 78228		

Aberdeen Proving Ground

Dir, USAMSAA
  ATTN: DRXSY-D
        DRXSY-MP, H. Cohen

Cdr, USATECOM
  ATTN: DRSTE-TO-F

Cdr, USA CSL/EA
  ATTN: A. Flatau, SAREA-DE-W
        Bldg E3516

Dir, Wpns Sys Concepts Team,
  Bldg. E3516, EA
  ATTN: DRDAR-ACW

USER EVALUATION OF REPORT

Please take a few minutes to answer the questions below; tear out this sheet and return it to Director, US Army Ballistic Research Laboratory, ARRADCOM, ATTN: DRDAR-TSB, Aberdeen Proving Ground, Maryland 21005. Your comments will provide us with information for improving future reports.

1. BRL Report Number _____

2. Does this report satisfy a need? (Comment on purpose, related project, or other area of interest for which report will be used.)

_____

_____

_____

3. How, specifically, is the report being used? (Information source, design data or procedure, management procedure, source of ideas, etc.)_____

_____

_____

4. Has the information in this report led to any quantitative savings as far as man-hours/contract dollars saved, operating costs avoided, efficiencies achieved, etc.? If so, please elaborate.

_____

_____

5. General Comments (Indicate what you think should be changed to make this report and future reports of this type more responsive to your needs, more usable, improve readability, etc.)_____

_____

_____

_____

6. If you would like to be contacted by the personnel who prepared this report to raise specific questions or discuss the topic, please fill in the following information.

            Name: _____

    Telephone Number: _____

Organization Address: _____

                      _____

                      _____